Numerical Simulation of Deformation and Failure Behavior of Geosynthetic Reinforced Soil Bridge Abutments

Yewei Zheng, A.M.ASCE[1]; Patrick J. Fox, F.ASCE[2]; and John S. McCartney, M.ASCE[3]

Abstract: This paper presents a numerical investigation of the deformation and failure behavior of geosynthetic reinforced soil (GRS) bridge abutments. The backfill soil was characterized using a nonlinear elastoplastic constitutive model that incorporates a hyperbolic stress–strain relationship with strain-softening behavior and the Mohr–Coulomb failure criterion. The geogrid reinforcement was characterized using a hyperbolic load–strain–time model. The abutments were numerically constructed in stages, including soil compaction effects, and then monotonically loaded in stages to failure. Simulation results indicate that a nonlinear reinforcement model is needed to characterize deformation behavior for high applied stress conditions. A parametric study was conducted to investigate the effects of reinforcement, backfill soil, and abutment geometry on abutment deformation and failure behavior. Results indicate that reinforcement vertical spacing, reinforcement stiffness, backfill soil friction angle, and lower GRS wall height are the most significant parameters. The shape of the failure surface is controlled primarily by abutment geometry and can be approximated as bilinear. **DOI:** **10.1061/(ASCE)GT.1943-5606.0001893.**

Author keywords: Geosynthetic reinforced soil; Bridge abutment; Numerical simulation; Service limit; Strength limit; Failure mechanism.

Introduction

Geosynthetic reinforced soil (GRS) bridge abutments are becoming widely used in transportation infrastructure and provide many advantages over traditional pile-supported designs, including lower cost, faster and easier construction, and smoother transition between the bridge and approach roadway. Several case histories for in-service GRS bridge abutments have been reported and show good field performance (Won et al. 1996; Wu et al. 2001; Abu-Hejleh et al. 2002; Adams et al. 2011b; Saghebfar et al. 2017). Numerical studies also have been conducted for GRS bridge abutments under service load conditions (Helwany et al. 2003, 2007; Zheng et al. 2014, 2015; Ambauen et al. 2015; Zheng and Fox 2016b, 2017; Ardah et al. 2017). These studies considered perfectly plastic soil and linearly elastic reinforcement and indicate relatively small lateral facing displacements and bridge seat settlements. Numerical modeling work on the deformation behavior and bearing capacity of GRS bridge abutments, associated with large deformations up to failure, is more limited and has also assumed perfectly plastic soil and linearly elastic reinforcement (Wu et al. 2006a, b). Based on other related research findings (e.g., Walters et al. 2002; Hatami and Bathurst 2006; Liu and Ling 2012; Yang et al. 2012; Zheng and Fox 2016a), strain softening of the backfill soil and nonlinear response of the geosynthetic reinforcement may be important for high applied stress conditions. An investigation considering these effects, including failure behavior, would represent a useful contribution to the literature.

This paper presents a numerical investigation of the deformation and failure behavior of GRS bridge abutments. Simulations were performed to identify the importance of strain-softening soil and nonlinear reinforcement behavior for a baseline case, and a parametric study was conducted to investigate the effects of reinforcement, backfill soil, and abutment geometry on abutment deformation and failure behavior. Results from this study provide insights with regard to the design of GRS bridge abutments for various loading conditions.

Background

Deformations, such as lateral facing displacements and vertical compressions, are important considerations in the design of GRS bridge abutments for the service limit condition, whereas bearing capacity is an important consideration for the strength limit condition. The Federal Highway Administration (FHWA) provides analytical and empirical design methods for both conditions (Adams et al. 2011a, b). The FHWA analytical method calculates ultimate bearing capacity based on the load-bearing capacity of soil-geosynthetic composite structures, and accounts for the maximum aggregate size and friction angle of the backfill soil and the vertical spacing and ultimate tensile strength of the geosynthetic reinforcement (Wu and Pham 2013; Wu et al. 2013). The allowable vertical stress for the service limit is then taken as 10% of the calculated ultimate bearing capacity (Nicks et al. 2013, 2016). The FHWA empirical method is based on a vertical stress–strain relationship that is measured from performance tests (e.g., GRS mini-pier loading tests) conducted using project-specific soil and geosynthetic materials (Adams et al. 2011a, b). In this case, the service limit is defined as an applied vertical stress of 200 kPa or the vertical stress at 0.5% vertical strain, and the strength limit is defined as the vertical stress at 5% vertical strain (Berg et al. 2009; Adams et al. 2011a, b; Nicks et al. 2013).

Field and laboratory loading tests have been conducted on large-scale GRS piers and abutments and generally indicate satisfactory

[1]Postdoctoral Research Scholar, Dept. of Structural Engineering, Univ. of California, San Diego, La Jolla, CA 92093-0085 (corresponding author). ORCID: https://orcid.org/0000-0001-9038-4113. Email: y7zheng@ucsd.edu

[2]Shaw Professor and Head, Dept. of Civil and Environmental Engineering, Pennsylvania State Univ., University Park, PA 16802. Email: pjfox@engr.psu.edu

[3]Associate Professor, Dept. of Structural Engineering, Univ. of California, San Diego, La Jolla, CA 92093-0085. Email: mccartney@ucsd.edu

Note. This manuscript was submitted on February 13, 2017; approved on January 3, 2018; published online on April 25, 2018. Discussion period open until September 25, 2018; separate discussions must be submitted for individual papers. This paper is part of the ***Journal of Geotechnical and Geoenvironmental Engineering***, © ASCE, ISSN 1090-0241.

performance under service loads and relatively high bearing capacity (Adams 1997; Gotteland et al. 1997; Ketchart and Wu 1997; Wu et al. 2001, 2006a; Adams et al. 2011a, 2014; Nicks et al. 2013, 2016; Iwamoto et al. 2015). Lee and Wu (2004) reviewed the results of several large-scale loading tests and suggested that bearing capacity can be as high as 900 kPa for closely spaced reinforcement and well-graded, well-compacted backfill soil. Nicks et al. (2013) conducted a series of performance tests on 2-m-high GRS mini-piers and found that reinforcement spacing and tensile strength have the most important effects on ultimate bearing capacity and that well-graded backfill materials and increasing levels of backfill compaction can increase the stiffness of a GRS mini-pier.

Wu et al. (2006a, b) conducted numerical simulations on the deformation behavior of GRS bridge abutments using a cap model for the backfill soil and a linearly elastic model for the geosynthetic reinforcement. In addition, they developed procedures to determine allowable vertical stress considering bridge seat type, reinforcement vertical spacing, and backfill soil properties. Leshchinsky (2014) and Xie and Leshchinsky (2015) performed a series of parametric studies using limit analysis to investigate the optimal reinforcement design and failure mechanism of GRS bridge abutments and found that reinforcement with closer vertical spacing in the upper section could efficiently increase the ultimate bearing capacity. Results also showed a curved failure surface extending downward from the heel of the bridge seat to the toe of the abutment for a bridge seat setback distance of 1.35 m or less and a compound failure surface for larger setback distances.

Numerical Model

The two-dimensional finite-difference program FLAC Version 7.0 was used for the current investigation. Zheng and Fox (2016b) developed a FLAC model to simulate the field performance of the Founders/Meadows GRS bridge abutment (Abu-Hejleh et al. 2000, 2001). Simulation results, including lateral facing displacements, bridge seat settlements, lateral and vertical earth pressures, and reinforcement tensile strains and forces, were in good agreement with field measurements at various stages of construction. Using a similar modeling approach, Zheng and Fox (2017) simulated the response of a geosynthetic reinforced soil-integrated bridge system (GRS-IBS) abutment and found good agreement with abutment vertical compression measurements reported by Adams et al. (2011b). Based on these results, Zheng and Fox (2016b, 2017) concluded that this type of numerical model has the capability to simulate the performance of GRS bridge abutments under service load conditions. In the current study, the model has been enhanced by incorporating strain-softening behavior for the backfill soil and nonlinear behavior for the geosynthetic reinforcement to simulate the deformation of GRS bridge abutments up to failure conditions. The explicit Lagrangian calculation method and mixed-discretization zoning technique used in FLAC are well suited for this purpose, with the ability to characterize plastic deformations and strain localization. FLAC is applicable for plane strain conditions, which represents a simplification for these three-dimensional structures.

Baseline Case

Geometry

The finite-difference grid and boundary conditions for the GRS bridge abutment baseline case are shown in Fig. 1. The model represents a single-span bridge system with span $L_b = 30$ m and symmetrical structures on both ends. Each end structure consists of a lower GRS wall and fill, bridge seat, upper GRS fill, and approach roadway. Only the right-hand side of the bridge system was simulated due to symmetry. The lower GRS wall has height $h = 5$ m and 25 modular facing blocks with dimensions of 0.3 m (length) × 0.2 m (height). An L-shaped bridge seat with a section thickness of 0.4 m rests on top of the lower GRS fill and has a setback distance of $a_b = 0.2$ m from the wall facing. The clear distance between the top facing block and bridge beam d_e is equal to the bridge seat thickness (0.4 m). The clearance height for the bridge beam above the foundation soil is 5.4 m, which satisfies the FHWA minimum requirement of 4.9 m for interstate highways (Stein and Neuman 2007). The bridge seat has an upper surface contact length of $L_c = 1.0$ m with the bridge beam and lower surface contact length of $L_s = 1.5$ m with the soil. There is a 100-mm-wide vertical expansion joint between the bridge beam and bridge seat. Assuming a ratio of bridge beam span to depth $R_{sd} = L_b/D = 20$, the depth of the bridge beam $D = 1.5$ m. A 1.8-m-high upper GRS fill lies behind the bridge seat and is overlain by a 0.1-m-thick concrete roadway. The reinforcement has a uniform length of $L_r = 3.5$ m ($0.7h$) and vertical spacing of $S_v = 0.2$ m for both the lower GRS fill and upper GRS fill. No secondary (i.e., bearing bed) reinforcement is included under the bridge seat for the baseline case.

To minimize the influence of boundary conditions on system response, the foundation soil has a depth of 10 m ($2h$), and the lateral boundary is located at a distance of 20 m ($4h$) from the wall facing. Lateral boundaries are fixed in the horizontal direction and are free to move in the vertical direction, whereas the bottom boundary is fixed in both the horizontal and vertical directions. Horizontal coordinate x is measured to the right from the back side of the wall facing, and vertical coordinate z is measured upward from the top surface of the foundation soil.

Soils

Zheng and Fox (2016b) simulated the static response of the Founders/Meadows GRS bridge abutment using a nonlinear elastoplastic model with a hyperbolic relationship and the Mohr–Coulomb failure criterion for the backfill soil. In the current investigation, the model is enhanced by incorporating strain-softening behavior at larger strain levels to simulate the response of GRS bridge abutments up to failure conditions. The tangent elastic modulus E_t, unloading–reloading modulus E_{ur}, bulk modulus B, and tangent Poisson's ratio ν_t are expressed as (Duncan et al. 1980)

$$E_t = \left[1 - \frac{R_f(1-\sin\phi')(\sigma_1' - \sigma_3')}{2c'\cos\phi' + 2\sigma_3'\sin\phi'}\right]^2 K p_a \left(\frac{\sigma_3'}{p_a}\right)^n \tag{1}$$

$$E_{ur} = K_{ur} p_a \left(\frac{\sigma_3'}{p_a}\right)^n \tag{2}$$

$$B = K_b p_a \left(\frac{\sigma_3'}{p_a}\right)^m \tag{3}$$

$$\nu_t = \frac{1}{2} - \frac{E_t}{6B} \tag{4}$$

where σ_1' and σ_3' = major and minor principal effective stresses; ϕ' = friction angle; c' = cohesion; R_f = failure ratio; K = elastic modulus number; n = elastic modulus exponent; p_a = atmospheric pressure; K_{ur} = unloading–reloading modulus number; K_b = bulk modulus number; m = bulk modulus exponent; and ν_t is limited to a range of 0–0.49. Eqs. (1)–(4) were implemented in FLAC using FISH subroutines to update the stress-dependent soil moduli during

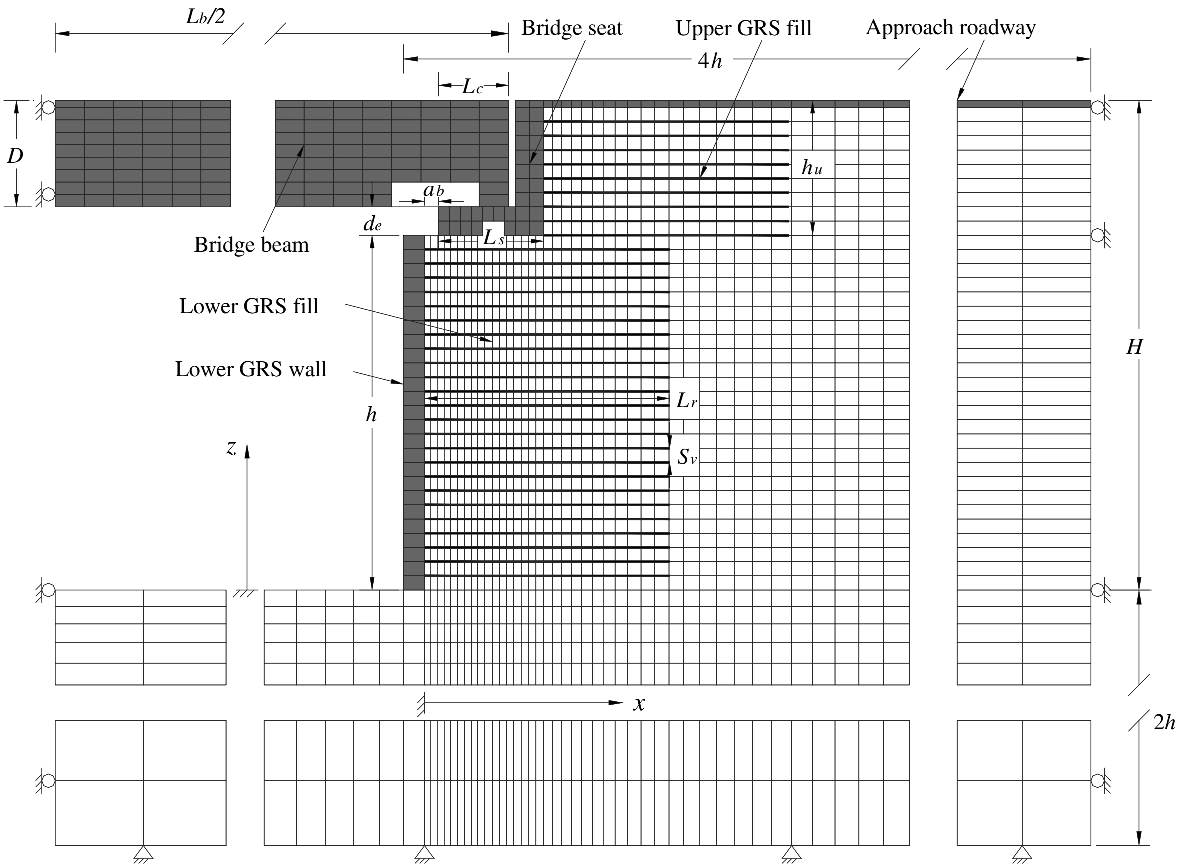

Fig. 1. Finite-difference grid and boundary conditions for GRS bridge abutment baseline case.

the course of each simulation. To account for strain-softening behavior, the friction angle and dilation angle were defined as piecewise linear functions of incremental plastic shear strain and calibrated using triaxial test data.

Backfill soil properties are based on measurements for a well-graded angular sand with maximum particle size $d_{\max} = 9.5$ mm, which meets the FHWA specifications for GRS bridge abutments (Berg et al. 2009; Adams et al. 2011a). Consolidated-drained triaxial compression tests were conducted on dry sand specimens at five levels of effective confining stress. The specimens were compacted at a relative density of 80% and unit weight $\gamma = 17.3$ kN/m^3. The tests were numerically simulated and soil parameters were back-calculated from the experimental results. The resulting piecewise linear relationships between incremental plastic shear strain ε_p, which occurs once the soil reaches the Mohr–Coulomb failure criterion, and the friction angle and dilation angle are shown in Fig. 2. The soil responds with peak values of friction angle and dilation angle of $\phi'_p = 46°$ and $\psi_p = 18°$, respectively, for $\varepsilon_p = 0$–4%. For $\varepsilon_p = 4$–15%, the soil experiences postpeak strain softening where both angles decrease linearly. For $\varepsilon_p \geq 15\%$, the soil responds with constant volume (i.e., steady state) friction angle and dilation angle of $\phi'_{cv} = 43°$ and $\psi_{cv} = 0°$, respectively. Using these relationships, a comparison of measured and simulated triaxial test results is shown in Fig. 3. The simulations slightly underestimate the peak deviator stress at lower confining stress levels; however, the nonlinear stress–strain behavior before peak strength and postpeak strain softening are characterized with good accuracy, especially for higher confining stresses. The simulated response for soil dilation behavior is also in good agreement with the measured data, especially for lower confining stress levels.

The foundation soil was specified as dense silty sandy gravel and simulated using a linearly elastic–perfectly plastic model with the Mohr–Coulomb failure criterion. A firm foundation soil was used for all simulations. A summary of parameters for the backfill soil and foundation soil is provided in Table 1.

Reinforcement

Geogrid reinforcement was included in the numerical model using cable elements rigidly connected to the facing blocks and characterized using the hyperbolic load–strain–time model proposed by Allen and Bathurst (2014a, b). Yu et al. (2016) also used this model and provided further discussion. Tensile force T is calculated from the product of tensile strain ε and a strain- and time-dependent secant stiffness J_s as

$$T = J_s \varepsilon \tag{5}$$

where

$$J_s = \frac{1}{\frac{1}{J_0} + \chi\varepsilon} \tag{6}$$

and J_0 = initial tangent stiffness; and χ = empirical fitting parameter, with both J_0 and χ expressed as functions of time t. Tangent stiffness J_t of the reinforcement is calculated as

$$J_t = \frac{1}{J_0(\frac{1}{J_0} + \chi\varepsilon)^2} \tag{7}$$

and the input parameter for elastic modulus is defined as

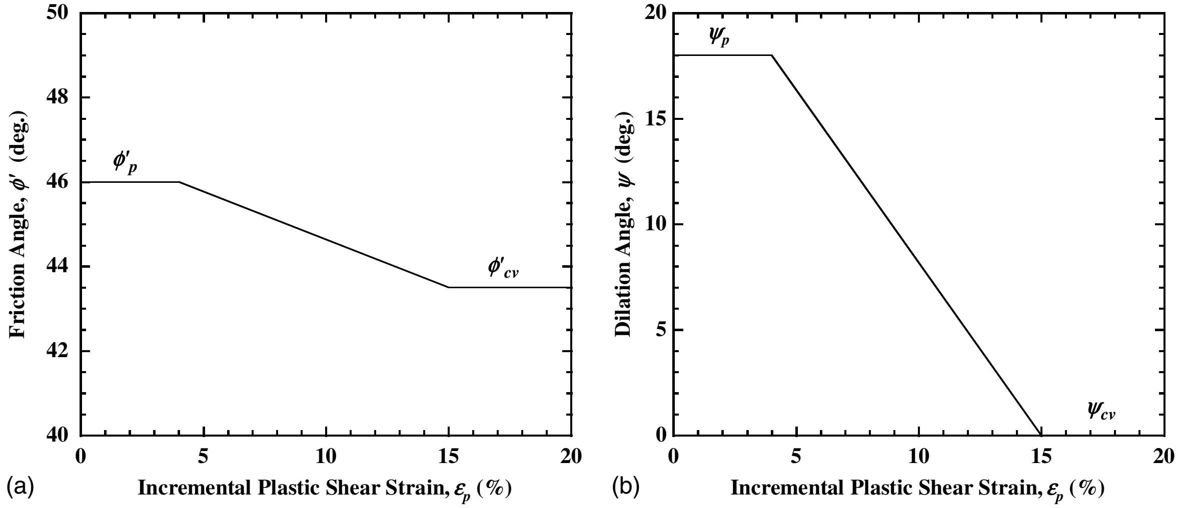

Fig. 2. Relationships for soil parameters: (a) friction angle; and (b) dilation angle.

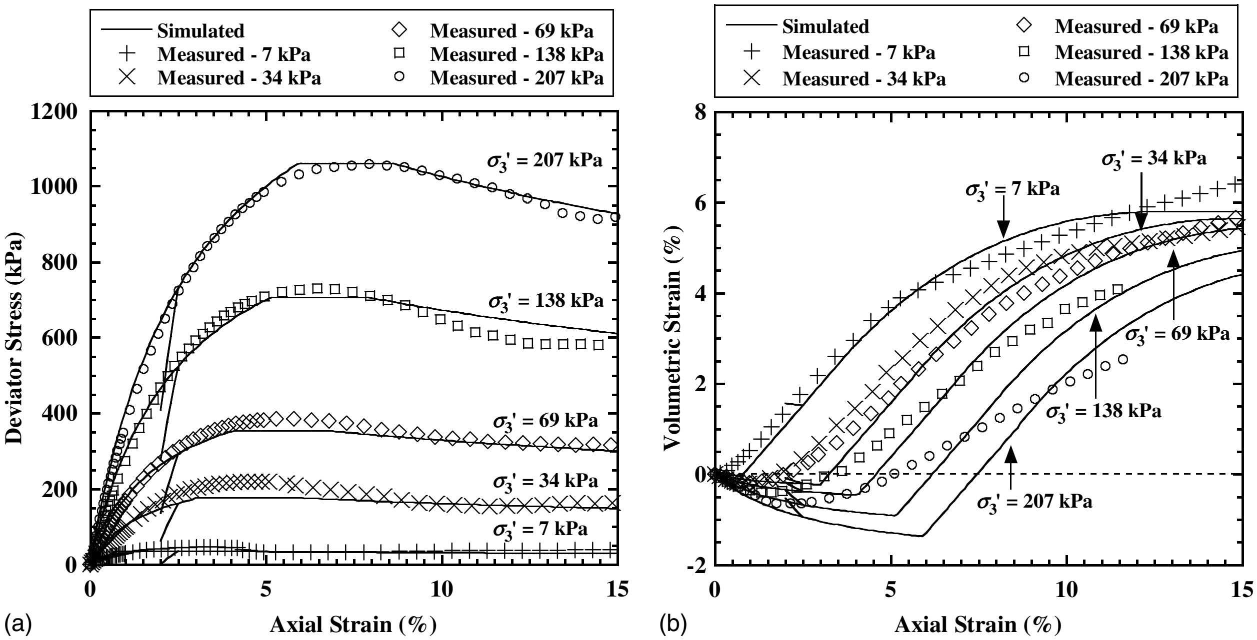

Fig. 3. Comparison of measured and simulated triaxial test results: (a) deviator stress; and (b) volumetric strain.

$$E_r = J_t/t_r \tag{8}$$

where t_r = geogrid thickness (constant).

A high-density polyethylene (HDPE) uniaxial geogrid was specified for the GRS bridge abutment, with properties and tensile behavior shown as Geogrid-2 in Fig. 4. The stiffness parameters are initial stiffness $J_0 = 1{,}054t^{-0.0697}$ kN/m and $\chi = 0.0359$ m/kN. Yu et al. (2016) reported that the stiffness values for several HDPE geogrids were not significantly affected by practical construction times of interest and, for simplicity, can be taken as constant during construction. Following this procedure, an end-of-construction time $t = 150$ days $= 3{,}600$ h was specified for the current simulations. As such, the tensile behavior for Geogrid-2 is characterized by $J_0 = 596$ kN/m and shows stiffness decreasing nonlinearly with increasing strain. A summary of parameters for Geogrid-2 is provided in Table 2. Geogrid-1 and Geogrid-3 are discussed later for the parametric study.

Structural Components

The concrete facing blocks, bridge seat, and roadway were modeled as linearly elastic materials with unit weight $\gamma = 23.5$ kN/m^3, elastic modulus $E = 20$ GPa, and Poisson's ratio $\nu = 0.2$. The bridge beam was modeled as a solid block ($L_b \times D \times 1$) of linearly elastic material with $E = 20$ GPa and $v = 0.2$. The unit weight of the bridge beam γ_b was changed to produce different values of applied load on the GRS bridge abutment. The vertical force per unit width on the lower GRS fill is $F_v = L_b D \gamma_b / 2$, and the corresponding average applied vertical stress is $q_v = F_v / L_s$.

Interfaces

Table 3 presents parameters for the various interfaces between soil, geogrid, facing block, bridge seat, and bridge beam. Soil–geogrid interfaces were included with the respective cable elements, whereas specific interface elements were needed to define block–block, soil–block, soil–bridge seat, and bridge beam–bridge

Table 1. Soil parameters

Property	Value
Backfill soil	
Unit weight, γ (kN/m^3)	17.3
Elastic modulus number, K	334
Unloading–reloading elastic modulus number, K_{ur}	401
Elastic modulus exponent, n	0.66
Failure ratio, R_f	0.67
Bulk modulus number, B	254
Bulk modulus exponent, m	0
Atmospheric pressure, p_a (kPa)	101.3
Cohesion, c' (kPa)	0
Peak friction angle, ϕ'_p (degrees)	46
Constant volume friction angle, ϕ'_{cv} (degrees)	43
Peak dilation angle, ψ_p (degrees)	18
Constant volume dilation angle, ψ_{cv} (degrees)	0
Foundation soil[a]	
Unit weight, γ (kN/m^3)	21.7
Elastic modulus, E (MPa)	80
Poisson's ratio, ν	0.3
Cohesion, c' (kPa)	2
Friction angle, ϕ' (degrees)	54
Dilation angle, ψ (degrees)	14

[a]From Yu et al. (2016).

seat interfaces. The soil–geogrid interfaces account for shear stiffness k_s, friction angle δ'_i, and adhesion c'_i, whereas the other interfaces account for these parameters and normal stiffness k_n in addition. Soil interface shear strengths were characterized using a reduction factor RF defined as

$$RF = \frac{\tan \delta'_i}{\tan \phi'_p} = \frac{c'_i}{c'} \tag{9}$$

Considering the typical embedment of wall facing at the toe of a GRS bridge abutment in the field, a relatively high toe shear stiffness of 40 MPa/m, as suggested by Yu et al. (2016), was selected for the interface between the lowermost facing block and foundation soil. The frictional interface between the bridge beam and bridge seat produces a lateral restraining force on the abutment structure, which can have an important effect on abutment deformations (Zheng and Fox 2016b).

Modeling Procedures

For each numerical simulation, the GRS bridge abutment model was constructed in stages and then monotonically loaded in stages to failure. Initially, the foundation soil was placed and resolved to equilibrium under gravitational forces. The lower GRS wall was

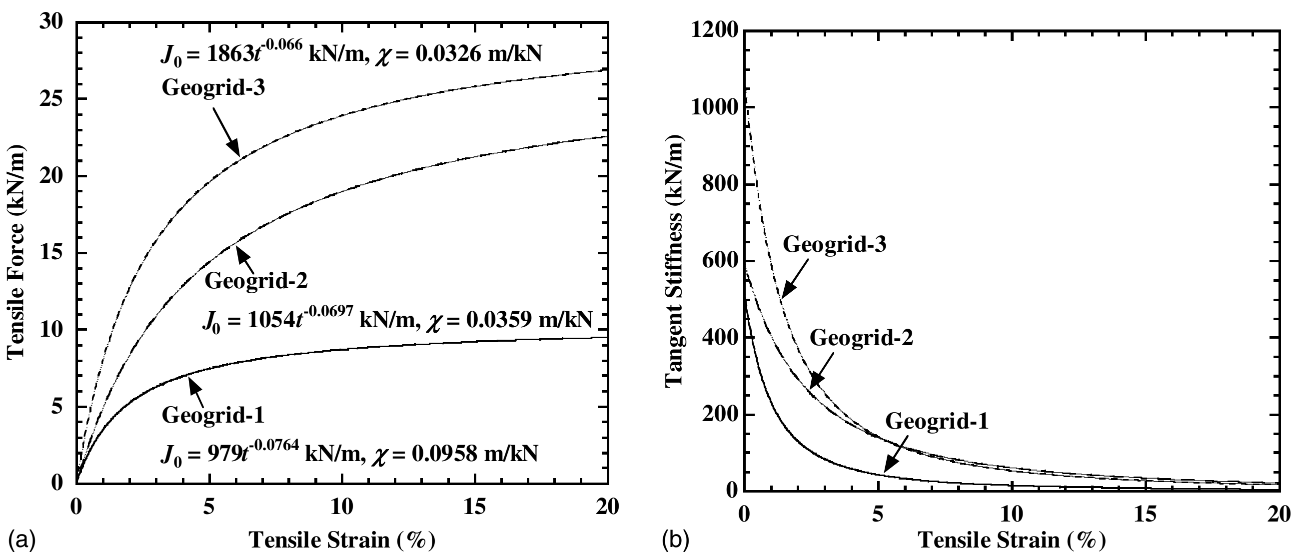

Fig. 4. Tensile behavior for three HDPE geogrids at $t = 3{,}600$ h: (a) tensile force; and (b) tangent stiffness (parameters from Yu et al. 2016).

Table 2. Reinforcement parameters

Property	Geogrid-1	Geogrid-2	Geogrid-3
Elastic modulus, E_r	Variable[a]	Variable[a]	Variable[a]
Cross-sectional area, A_r	0.002 m^2	0.002 m^2	0.002 m^2
Thickness, t_r	2 mm	2 mm	2 mm
Tensile strength at 5% strain, $T_{5\%}$[b]	27 kN/m	31 kN/m	52 kN/m
Ultimate tensile strength, T_{ult}[b]	58 kN/m	70 kN/m	114 kN/m
Initial tensile stiffness, J_0[c]	524 kN/m	596 kN/m	1,085 kN/m
Fitting parameter, χ[c]	0.0958 m/kN	0.0359 m/kN	0.0326 m/kN

[a]Calculated using Eqs. (7) and (8) based on parameters reported by Yu et al. (2016).
[b]Provided by manufacturer.
[c]Calculated for $t = 3{,}600$ h.

Table 3. Interface parameters

Property	Soil–geogrid	Soil–block/bridge seat	Block–block	Bridge beam–bridge seat
Normal stiffness, k_n	—	1,000 MPa/m	100,000 MPa/m	100,000 MPa/m
Shear stiffness, k_s	1 MN/m/m	1 MPa/m	40 MPa/m	40 MPa/m
Friction angle, δ_i'	41.4° [a]	33.9° [b]	36.0° [c]	21.8° [d]
Adhesion, c_i'	0	0	58 kPa[c]	0

[a]Based on average of data ($RF = 0.85$) from Vieira et al. (2013).
[b]Based on data ($RF = 0.65$) from Ling et al. (2010).
[c]Based on Yu et al. (2016).
[d]Based on a friction coefficient of 0.4 for bearing pads from Caltrans (1994).

constructed in layers on top of the foundation soil, with each layer consisting of one soil lift, one facing block, and the necessary interfaces. Geogrid reinforcement layers were placed at specified elevations, depending on the simulation. Following Hatami and Bathurst (2006), Guler et al. (2007), Zheng and Fox (2017), and Zheng et al. (2017), a temporary uniform surcharge stress of 8 kPa was applied to the top surface of each soil lift to simulate the effect of compaction and then removed prior to application of the next lift. On removal of the surcharge stress, the soil follows an unloading path with higher stiffness, which is similar to the paths for axisymmetric unloading shown as examples for the simulated stress–strain relationships in Fig. 3(a). Reloading follows the same path, and as such, each soil lift has an initially stiffer response during placement of the next lift. Once the lower GRS wall was completed, the bridge seat was placed, the upper GRS fill was similarly constructed in layers behind the bridge seat, and the approach roadway was placed on the surface. The bridge beam was then placed on the bridge seat with an initial unit weight of $\gamma_b = 3.34\ \mathrm{kN/m^3}$, which was chosen to produce an initial average applied vertical stress of $q_v = 50$ kPa. During subsequent loading, the unit weight of the bridge beam was increased in stages to produce failure of the abutment. For each construction and loading stage, the numerical model was resolved to equilibrium under gravitational forces. Abutment failure was assumed to occur if FLAC could not converge to equilibrium or the lower GRS fill reached a vertical strain of 10%.

Results from the numerical simulations are assessed at conditions of service limit and strength limit for the GRS bridge abutment. Similar to Nicks et al. (2013, 2016), the service limit is defined according to two criteria. The first criterion is an average applied vertical stress of $q_v = 200$ kPa, and the second criterion is an average vertical strain of $\varepsilon_v = 0.5\%$, where ε_v is based on abutment compression (i.e., compression of lower GRS fill) defined as the difference between the average downward displacement of the bridge seat and the average downward displacement of the underlying foundation soil. The strength limit is defined as an average vertical strain of $\varepsilon_v = 5\%$ and is based on considerations of ultimate bearing capacity as per FHWA guidelines (Nicks et al. 2013).

Perfectly Plastic Soil and Linearly Elastic Reinforcement Cases

In addition to the baseline case defined by the aforementioned modeling conditions and parameters, simulations were also performed for two additional cases to investigate the effects of soil strain-softening and nonlinear reinforcement behavior on the deformation response. The first additional case assumes perfectly plastic soil (PPS) with constant values of friction angle and dilation angle ($\phi' = 46°$ and $\psi = 18°$) and nonlinear reinforcement (as per the baseline case). The second additional case assumes linearly elastic reinforcement (LER) with constant stiffness equal to the secant stiffness at 5% tensile strain $J_{5\%} = 620$ kN/m and strain-softening soil (as per the baseline case).

Simulation Results

Profiles of lateral facing displacement for the baseline, PPS, and LER cases and two levels of average applied vertical stress $q_v = 400$ kPa and $q_v = 800$ kPa are presented in Fig. 5(a). At

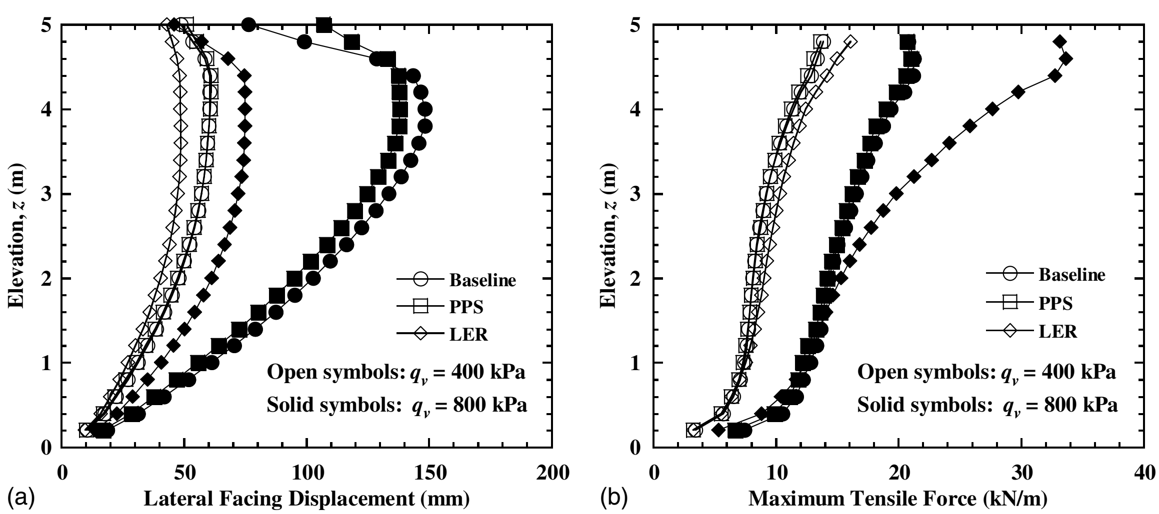

Fig. 5. Simulation results: (a) lateral facing displacement; and (b) maximum tensile force in reinforcement.

J. Geotech. Geoenviron. Eng., 2018, 144(7): 04018037

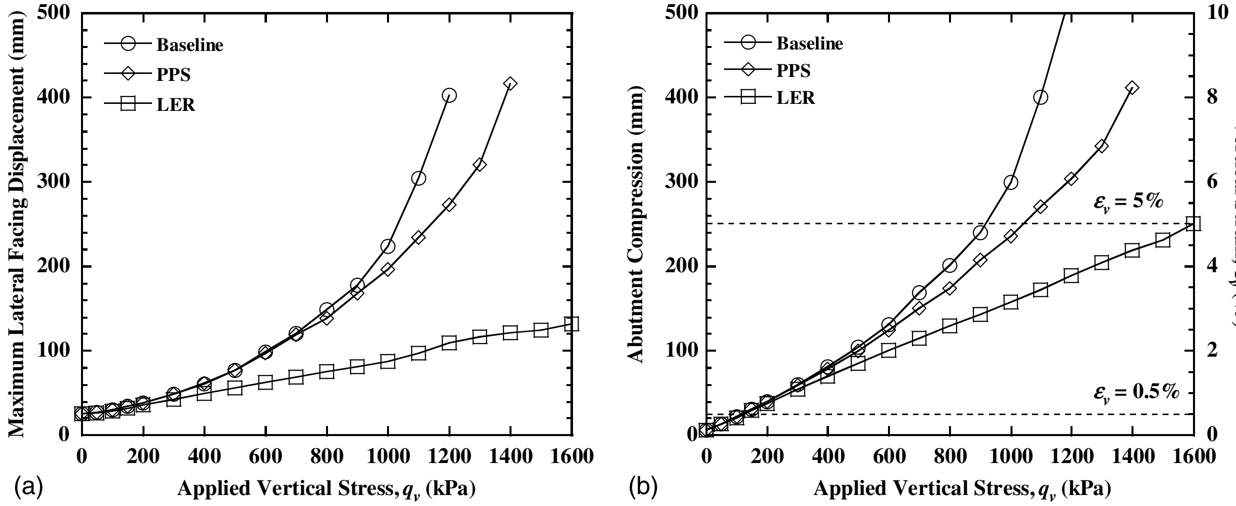

Fig. 6. Simulation results: (a) maximum lateral facing displacement; and (b) abutment compression and vertical strain.

$q_v = 400$ kPa for the baseline case, a maximum lateral displacement of 60.6 mm occurs near the top of the wall at an elevation of $z = 4.2$ m above the foundation soil. Lateral displacements for the baseline and PPS cases are in close agreement and larger than for the LER case. At $q_v = 800$ kPa, lateral displacements increase significantly and the trends are similar. The baseline case yields the largest lateral displacements with a maximum value of 148.4 mm at $z = 4.0$ m. Maximum lateral displacements for the PPS and LER cases are 138.0 and 75.0 mm, respectively. Corresponding profiles of maximum tensile force in the geogrid reinforcement are presented in Fig. 5(b). For the baseline case and $q_v = 400$ kPa, the highest tensile force (13.9 kN/m) occurs at $z = 4.8$ m with an associated tensile strain of 4.7%. The factor of safety (FS) against reinforcement rupture is 5.0, based on the ultimate tensile strength $T_{ult} = 70$ kN/m (Table 2). For the PPS and LER cases, the highest tensile forces are 13.7 and 16.1 kN/m, and FS = 5.1 and 4.3, respectively. Maximum tensile forces for the baseline and PPS cases are in close agreement and slightly smaller than for the LER case. At $q_v = 800$ kPa, maximum tensile forces increase significantly and the trends are similar; however, maximum tensile forces for the LER case are much larger than for the baseline and PPS cases near the top of the wall. The highest tensile force for the baseline case of 21.3 kN/m occurs at $z = 4.6$ m with an associated tensile strain of 14.4% and FS = 3.3. Highest tensile forces are 21.0 and 33.6 kN/m for the PPS and LER cases, respectively, with corresponding values of FS = 3.3 and FS = 2.1.

The results of Fig. 5 show that, at the higher applied vertical stress $q_v = 800$ kPa, lateral displacements and maximum tensile forces are nearly equal for the baseline and PPS cases. This suggests that postpeak strain-softening behavior for the soil is not a critical consideration for the conditions simulated. On the other hand, lateral displacements are much lower and maximum tensile forces are much higher for the LER case, which suggests that the geosynthetic constitutive model (i.e., linear versus nonlinear) has a significant effect. Reinforcement stiffness is constant for the LER case and decreases significantly with increasing strain for the baseline and PPS cases (Fig. 4). As the applied vertical stress on the abutment increases and soil stiffness decreases, the reinforcement experiences less extension and picks up a greater fraction of this load for the LER case.

Plots of maximum lateral facing displacement, average abutment compression, and corresponding average abutment vertical strain (ε_v) versus average applied vertical stress (q_v) for the three simulation cases are shown in Fig. 6. In general, the results indicate that the baseline and PPS cases display nonlinear responses, whereas the LER case shows a nearly linear response. On both plots, deformations are essentially equal for the baseline and PPS cases for $q_v \leq 600$ kPa because the soil has not yet reached a strain-softening condition. Beyond 600 kPa, the baseline case indicates lower stiffness than the PPS case. Deformations for the LER case are close to the baseline case for $q_v \leq 200$ kPa and then deviate substantially with increasing applied vertical stress. This suggests that, for the conditions simulated, a LER model can capture the deformation behavior of GRS bridge abutments at the service limit but not for higher applied stress levels approaching failure. As such, the selection of a constant reinforcement stiffness value may be difficult. In the current study, the $J_{5\%}$ value (620 kN/m) gives good accuracy for $q_v \leq 200$ kPa.

Based on the data in Fig. 6, Table 4 provides values of maximum lateral facing displacement $\Delta_{h,200}$ and average abutment compression $\Delta_{v,200}$ at the service limit of $q_v = 200$ kPa, vertical stress $q_{0.5\%}$ at the service limit of $\varepsilon_v = 0.5\%$, and vertical stress $q_{5\%}$ at the strength limit of $\varepsilon_v = 5\%$. Consistent with the trends in Fig. 5, the service limit values indicate essentially no effect for strain-softening soil and a relatively minor effect for nonlinear reinforcement. In comparison, FHWA guidelines (Nicks et al. 2013) specify the allowable vertical stress at the service limit $q_{0.5\%}$ as 10% of the ultimate bearing capacity q_{ult} (Wu and Pham 2013; Wu et al. 2013), where q_{ult} is calculated as

$$q_{ult} = \left[\sigma_c' + 0.7^{\frac{S_v}{6d_{\max}}}\left(\frac{T_{ult}}{S_v}\right)\right]K_p + 2c'\sqrt{K_p} \tag{10}$$

Table 4. Deformations and vertical stresses for three simulation cases at service limit and strength limit

Case	Service limit $\Delta_{h,200}$ (mm)	Service limit $\Delta_{v,200}$ (mm)	Service limit $q_{0.5\%}$ (kPa)	Strength limit $q_{5\%}$ (kPa)
Baseline	38.0	33.6	118	917
Perfectly plastic soil (PPS)	38.0	33.6	118	1,043
Linearly elastic reinforcement (LER)	35.2	31.3	127	1,600

J. Geotech. Geoenviron. Eng., 2018, 144(7): 04018037

where σ_c' = effective confining stress (typically taken as zero to be conservative); and K_p = Rankine passive earth pressure coefficient. Using Eq. (10) and $\sigma_c' = 0$, the calculated value of $q_{0.5\%}$ is 61 kPa for the baseline case, which is approximately one-half of the simulated value (118 kPa). Similar conservative results using Eq. (10) were reported by Nicks et al. (2016) for loading tests on GRS mini-piers constructed using a well-graded soil. At the strength limit of $\varepsilon_v = 5\%$, the PPS simulation yielded a higher vertical stress by 14% and the LER simulation yielded a higher vertical stress by 75% than the baseline case. Thus, beyond the service limit, the effects of strain-softening soil and nonlinear reinforcement can become significant, and both should be taken into account as needed.

Parametric Study

A parametric study was conducted to investigate the effects of various reinforcement, backfill soil, and geometry parameters on the deformation behavior of GRS bridge abutments. The variables are reinforcement vertical spacing, reinforcement stiffness, reinforcement length, secondary reinforcement, backfill soil cohesion, backfill soil friction angle, backfill soil dilation angle, bridge seat setback distance, bridge seat length, and lower GRS wall height. For each series of simulations, only the variable of interest was changed and the other variables were held constant and equal to the baseline case. Results are presented for maximum lateral facing displacement of the lower GRS wall, and vertical compression and strain of the abutment (i.e., lower GRS fill) with increasing average applied vertical stress. A summary of values obtained at the service limit and strength limit is presented in Table 5.

Reinforcement Vertical Spacing

Numerical simulations were conducted for reinforcement vertical spacing: $S_v = 0.2$, 0.4, and 0.6 m. In each case, a soil lift thickness of 0.2 m was maintained for the numerical construction procedure. Fig. 7 indicates that abutment deformations increase significantly with increasing reinforcement spacing. For instance, at the service limit of $q_v = 200$ kPa, $\Delta_{h,200}$ increases from 38.0 to 93.6 mm and $\Delta_{v,200}$ increases from 33.6 to 70.2 mm when S_v increases from 0.2 to 0.6 m. At the service limit of $\varepsilon_v = 0.5\%$, the value of $q_{0.5\%} =$ 118 kPa for $S_v = 0.2$ m is nearly twice that for $S_v = 0.6$ m

Table 5. Results from parametric study at service limit and strength limit

Variable	Case	Service limit			Strength limit
		$\Delta_{h,200}$ (mm)	$\Delta_{v,200}$ (mm)	$q_{0.5\%}$ (kPa)	$q_{5\%}$ (kPa)
Reinforcement vertical spacing	0.2 m	38.0	33.6	118	917
	0.4 m	60.5	48.0	82	519
	0.6 m	93.6	70.2	65	364
Reinforcement stiffness	Geogrid-1	47.6	41.5	104	500
	Geogrid-2	38.0	33.6	118	917
	Geogrid-3	30.7	28.8	143	1,121
Reinforcement length	0.3h	65.4	46.8	101	523
	0.5h	40.3	34.5	115	898
	0.7h	38.0	33.6	118	917
	0.9h	37.5	33.5	119	925
	1.1h	37.5	33.5	119	948
Secondary reinforcement layers	0	38.0	33.6	118	917
	5	37.0	32.7	123	1,007
	10	35.0	31.6	127	1,117
	15	34.0	30.9	131	1,232
Backfill soil cohesion	0 kPa	38.0	33.6	118	917
	5 kPa	35.3	32.7	124	940
	10 kPa	33.6	31.5	127	975
	15 kPa	33.0	31.0	135	1008
Backfill soil friction angle	38°	51.4	40.7	99	682
	42°	43.7	36.9	108	805
	46°	38.0	33.6	118	917
	50°	34.3	31.2	127	1,059
Backfill soil dilation angle	6°	39.4	39.7	105	777
	12°	38.7	36.0	113	852
	18°	38.0	33.6	118	917
	24°	38.0	32.3	123	968
Bridge seat setback distance	0.2 m	38.0	33.6	118	917
	0.6 m	40.0	32.5	131	962
	1.0 m	39.1	30.8	146	1,040
	1.4 m	38.5	28.2	157	1,127
Bridge seat length	1.0 m	35.4	29.0	127	983
	1.5 m	38.0	33.6	118	917
	2.0 m	40.9	37.7	115	907
	2.5 m	42.3	38.5	115	980
Lower GRS wall height	3.0 m	26.7	23.9	143	926
	5.0 m	38.0	33.6	118	917
	7.0 m	49.2	39.9	137	1,008
	9.0 m	60.6	43.1	158	1,049

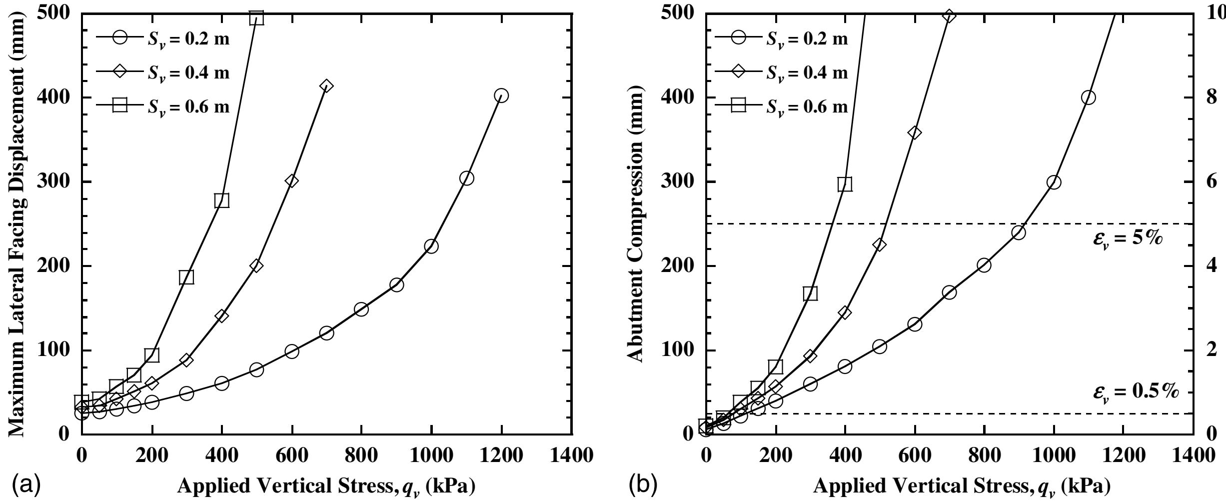

Fig. 7. Effect of reinforcement vertical spacing: (a) maximum lateral facing displacement; and (b) abutment compression and vertical strain.

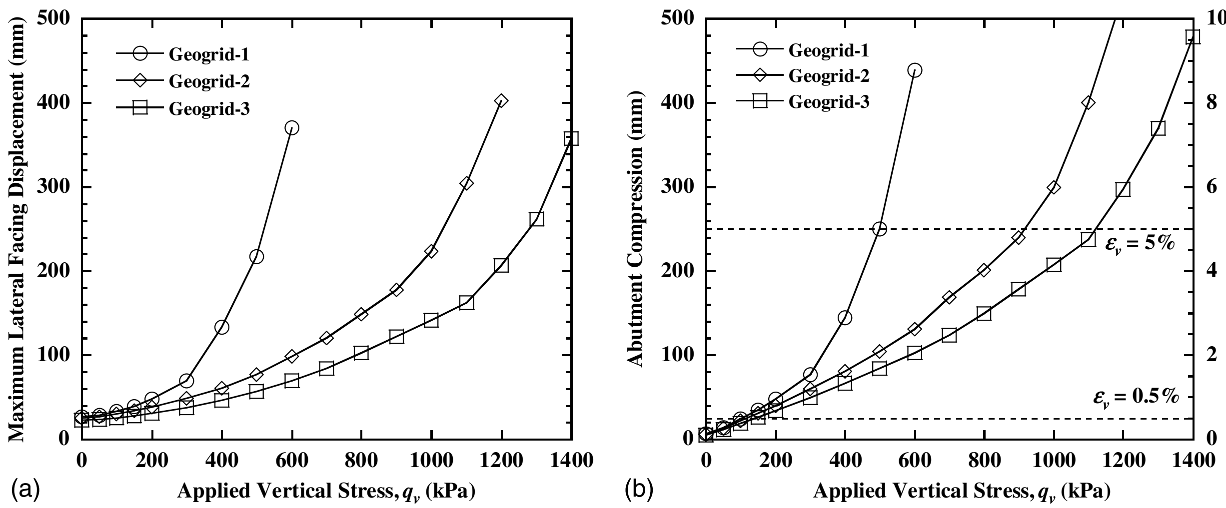

Fig. 8. Effect of reinforcement stiffness: (a) maximum lateral facing displacement; and (b) abutment compression and vertical strain.

(65 kPa). At the strength limit, $q_{5\%}$ decreases significantly and nonlinearly from 917 to 519 to 364 kPa when S_v increases from 0.2 to 0.4 to 0.6 m.

Reinforcement Stiffness

Simulations were conducted for three HDPE geogrids, Geogrid-1, Geogrid-2 (baseline case), and Geogrid-3, as originally described by Yu et al. (2016). Material properties are provided in Table 2, and nonlinear tensile behavior is illustrated in Fig. 4. Geogrid-1 has the lowest stiffness, Geogrid-2 is intermediate, and Geogrid-3 has the highest stiffness. Fig. 8 indicates that the maximum lateral facing displacement and vertical compression of the abutment decrease significantly with increasing reinforcement stiffness. At $q_v = 200$ kPa, $\Delta_{h,200}$ decreases from 47.6 to 30.7 mm and $\Delta_{v,200}$ decreases from 41.5 to 28.8 mm when reinforcement changes from Geogrid-1 to Geogrid-3. Correspondingly, $q_{0.5\%}$ increases from 104 to 143 kPa and $q_{5\%}$ increases from 500 to 1121 kPa.

Reinforcement Length

Abutment deformations for reinforcement lengths of $L_r = 0.3$, 0.5, 0.7, 0.9, and $1.1h$ are presented in Fig. 9 and decrease only slightly with increasing reinforcement length for $L_r \geq 0.5h$, which is consistent with the findings of Zheng and Fox (2016b) for service load conditions. At the strength limit, $q_{5\%}$ increases from 898 to 948 kPa when L_r increases from 0.5 to $1.1h$. For $L_r = 0.3h$ (=1.5 m), deformations are much larger than for the other cases, and failure occurs at a lower applied vertical stress (523 kPa). In this case, the reinforcement does not extend beyond the failure surface, which intersects the heel of the bridge seat at the top of the lower GRS fill (distance from wall facing $x = 1.7$ m).

Secondary Reinforcement

Secondary reinforcement layers are often included below the bridge seat to provide additional support and are specified for the GRS-IBS design method (Adams et al. 2011a). In the current study, numerical simulations were conducted for secondary reinforcement layer numbers $n_{sr} = 0$, 5, 10, and 15, where $n_{sr} = 0$ indicates no secondary reinforcement and $n_{sr} = 15$ indicates 15 layers of secondary reinforcement between elevations $z = 2.0$ and 5.0 m. The secondary reinforcement layers have a length of $L_s + 2a_b$ (= 1.9 m) and are not connected to the facing blocks. The results are presented in Fig. 10 and show that, when n_{sr} increases from 0 to

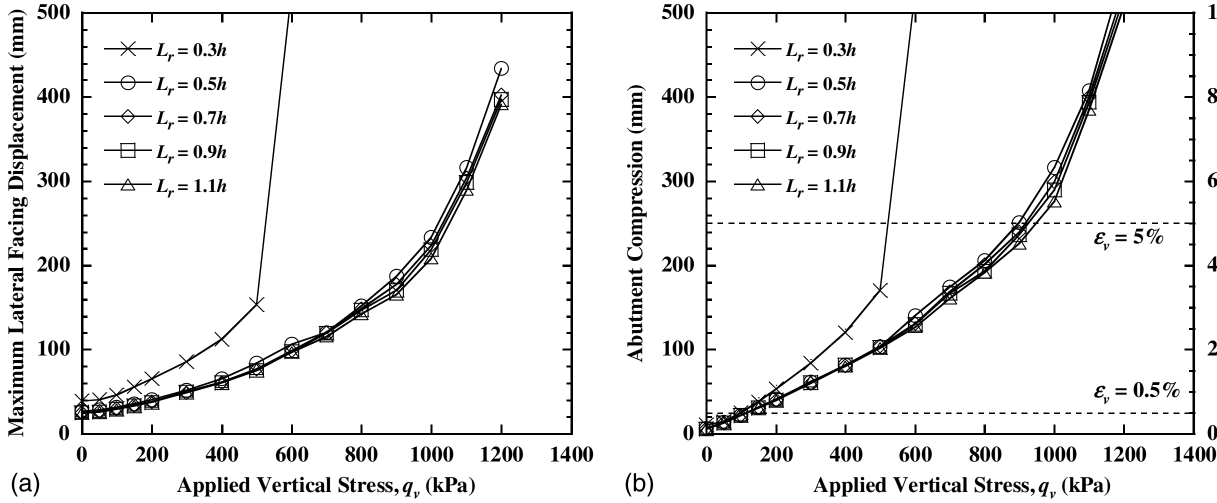

Fig. 9. Effect of reinforcement length: (a) maximum lateral facing displacement; and (b) abutment compression and vertical strain.

15, abutment deformations are only slightly reduced for $q_v \leq 200$ kPa. At higher stress levels, abutment deformations decrease significantly with an increasing number of secondary reinforcement layers. For example, at the strength limit, $q_{5\%}$ increases from 917 kPa for $n_{sr} = 0$ to 1,232 kPa for $n_{sr} = 15$. These results are consistent with the findings from large-scale loading tests on GRS mini-piers, which indicate that secondary reinforcement is unlikely to reduce abutment compression for service loads but can increase the ultimate bearing capacity (Nicks et al. 2013).

Backfill Soil Cohesion

Backfill soil can display apparent cohesion due to unsaturated conditions, which may be significant depending on the fines content and the shape of the soil-water retention curve. Abutment deformations for backfill soil cohesion $c' = 0$, 5, 10, and 15 kPa are presented in Fig. 11. Corresponding values of adhesion for soil–block and soil–geogrid interfaces were obtained using Eq. (9). The effect of increasing cohesion on abutment deformations is small for service limit conditions and becomes more important at higher stress levels. As the cohesion increases from 0 to 15 kPa, $q_{0.5\%}$ increases from 118 to 135 kPa and $q_{5\%}$ increases from 917 to 1,008 kPa.

Backfill Soil Friction Angle

Simulations were conducted for backfill soil friction angles of $\phi'_p = 38°$, 42°, 46°, and 50°, with $\phi'_{cv} = 35°$, 39°, 43°, and 47°, respectively. Corresponding friction angles for soil–block and soil–geogrid interfaces were obtained using Eq. (9). The results in Fig. 12 indicate that friction angle has a significant effect on abutment deformations, including both the service limit and strength limit conditions. For instance, $\Delta_{h,200}$ decreases from 51.4 to 34.3 mm and $\Delta_{v,200}$ decreases from 40.7 to 31.2 mm when ϕ'_p increases from 38° to 50°. Correspondingly, $q_{0.5\%}$ increases from 99 to 127 kPa at a service limit of $\varepsilon_v = 0.5\%$ and $q_{5\%}$ increases from 682 to 1,059 kPa at a strength limit of $\varepsilon_v = 5\%$.

Backfill Soil Dilation Angle

Simulations were conducted for soil dilation angles of $\psi_p = 6°$, 12°, 18°, and 24°, and the results are presented in Fig. 13. In general, maximum lateral facing displacements are not significantly affected by dilation angle. Conversely, abutment vertical compression decreases with increasing ψ_p, especially at higher stress levels. For instance, at the strength limit, $q_{5\%}$ increases from 777 to 968 kPa when ψ_p increases from 6 to 24°.

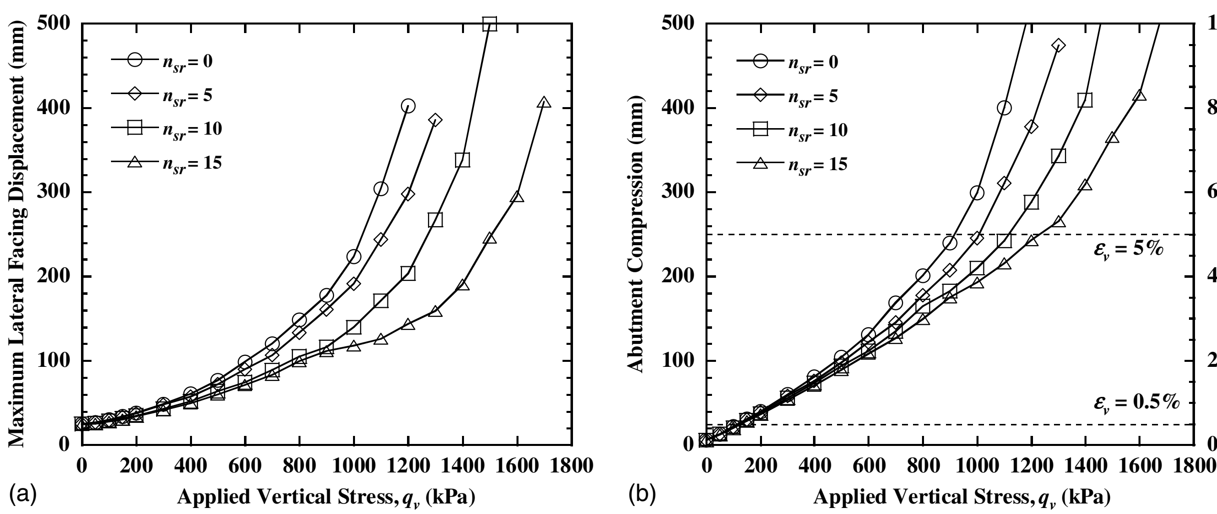

Fig. 10. Effect of secondary reinforcement: (a) maximum lateral facing displacement; and (b) abutment compression and vertical strain.

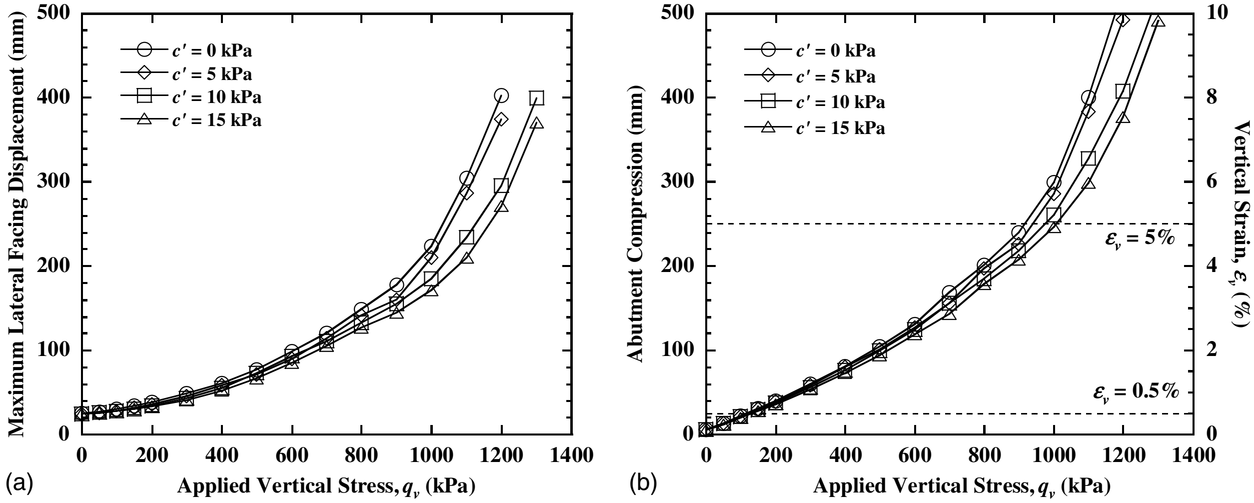

Fig. 11. Effect of backfill soil cohesion: (a) maximum lateral facing displacement; and (b) abutment compression and vertical strain.

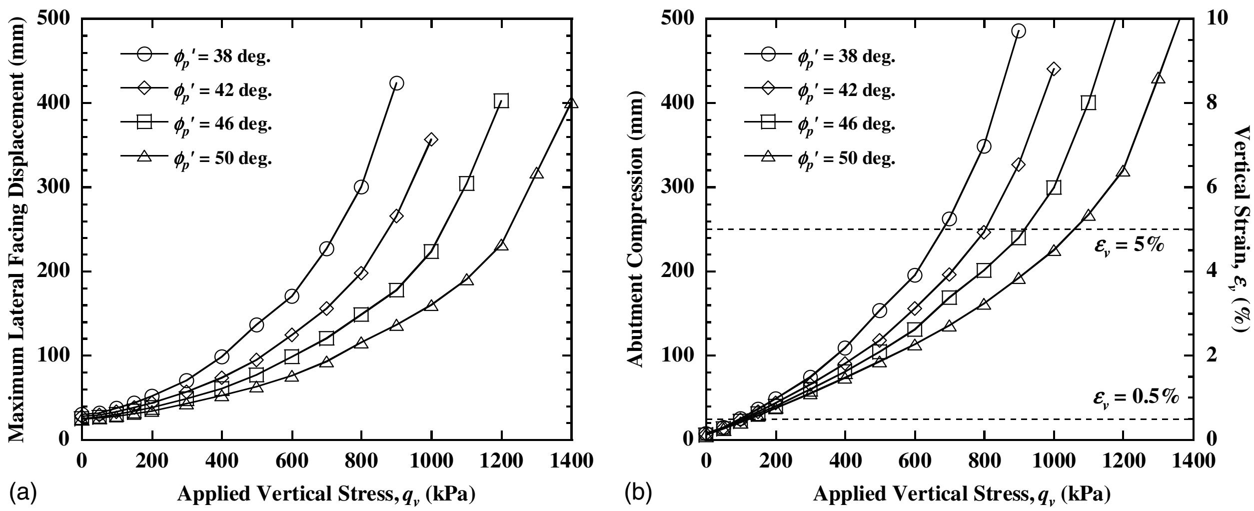

Fig. 12. Effect of backfill soil friction angle: (a) maximum lateral facing displacement; and (b) abutment compression and vertical strain.

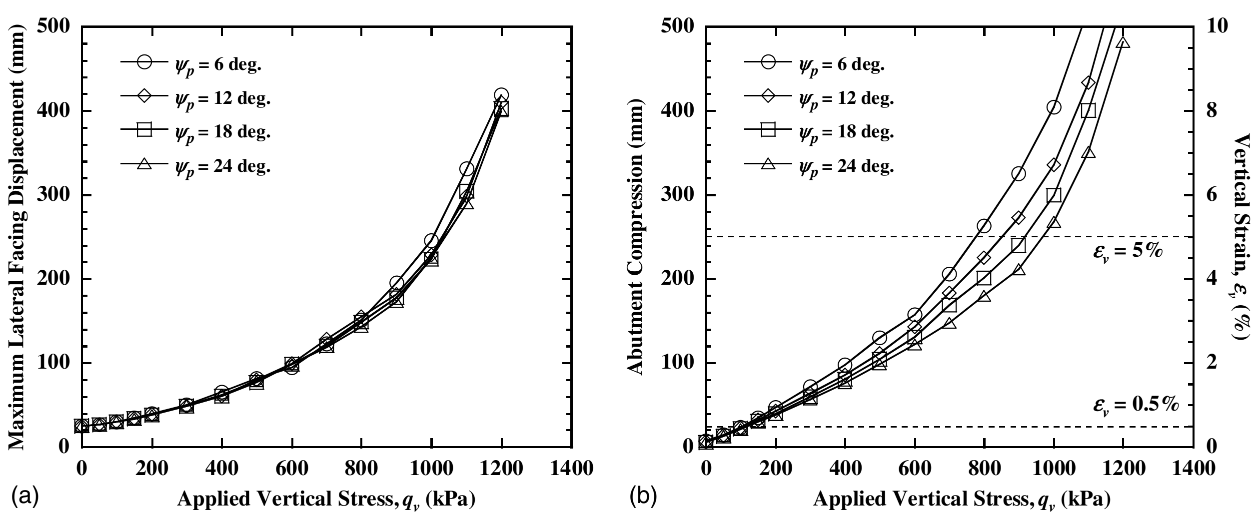

Fig. 13. Effect of backfill soil dilation angle: (a) maximum lateral facing displacement; and (b) abutment compression and vertical strain.

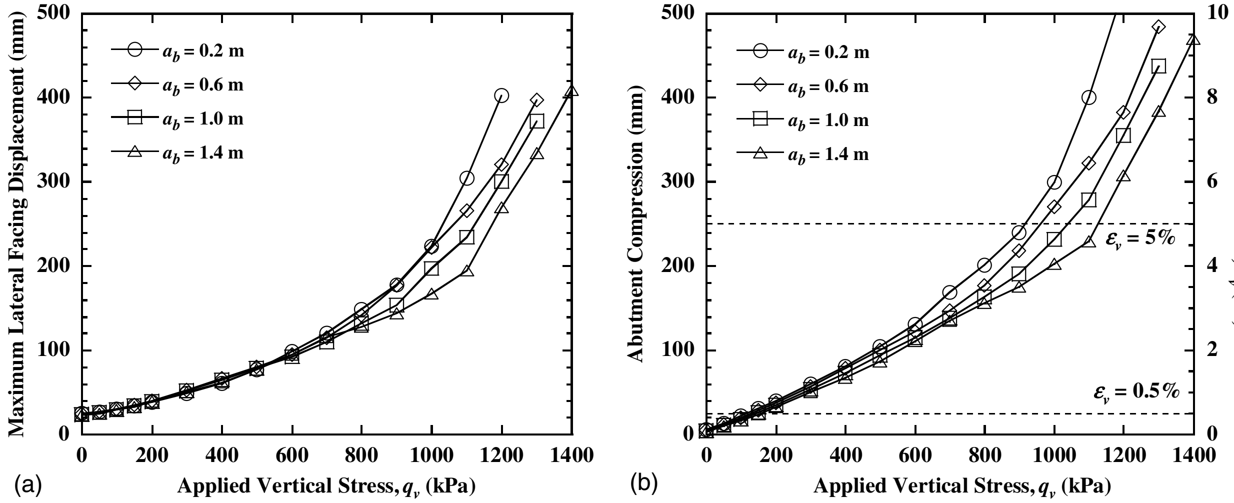

Fig. 14. Effect of bridge seat setback distance: (a) maximum lateral facing displacement; and (b) abutment compression and vertical strain.

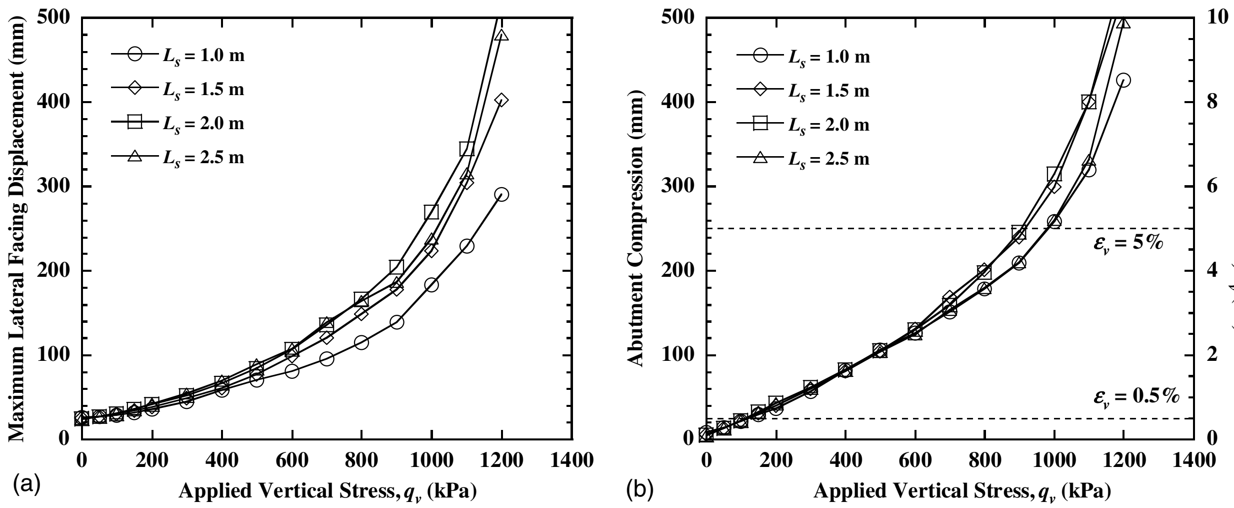

Fig. 15. Effect of bridge seat length: (a) maximum lateral facing displacement; and (b) abutment compression and vertical strain.

Bridge Seat Setback Distance

Abutment deformations for bridge seat setback distance $a_b = 0.2$, 0.6, 1.0, and 1.4 m are presented in Fig. 14. Bridge seat setback has little effect on maximum lateral facing displacement for $q_v \leq 600$ kPa, whereas these values decrease with increasing a_b at higher applied vertical stress levels. Similarly, abutment vertical compression decreases and $q_{5\%}$ increases from 917 to 1,127 kPa as a_b increases from 0.2 to 1.4 m. The effect of bridge seat setback is insignificant for service limit conditions.

Bridge Seat Length

Abutment deformations for bridge seat lengths $L_s = 1.0$, 1.5, 2.0, and 2.5 m are presented in Fig. 15. Bridge seat length has little effect for service limit conditions. At higher stress levels, the maximum lateral facing displacement and abutment compression generally increase with increasing L_s. At the strength limit, $q_{5\%}$ decreases nonlinearly from 983 to 917 to 907 kPa when L_s increases from 1.0 to 1.5 to 2.0 m. However, for $L_s = 2.5$ m, the maximum lateral displacement curve is similar to $L_s = 1.5$ m and the abutment compression curve is similar to $L_s = 1.0$ m.

Lower GRS Wall Height

Numerical simulations were conducted for GRS bridge abutments with lower GRS wall heights $h = 3$, 5, 7, and 9 m. Figs. 16 (a and b) indicate that maximum lateral facing displacement and abutment compression increase with increasing lower GRS wall height. For example, at $q_v = 200$ kPa, $\Delta_{h,200}$ increases from 26.7 to 60.6 mm and $\Delta_{v,200}$ increases from 23.9 to 43.1 mm when h increases from 3 to 9 m. Normalized relationships for maximum lateral facing displacement divided by h are shown in Fig. 16(c). The four relationships essentially converge for $q_v \leq 200$ kPa and thus indicate that maximum lateral facing displacements are proportional to lower GRS wall height for service limit conditions. Interestingly, at higher applied stress levels, normalized maximum lateral facing displacement decreases as h increases from 3 to 9 m for the same applied vertical stress. Corresponding vertical strain relationships, in which abutment vertical compression is normalized by h, are presented in Fig. 16(d) and show similar trends. Thus, taller

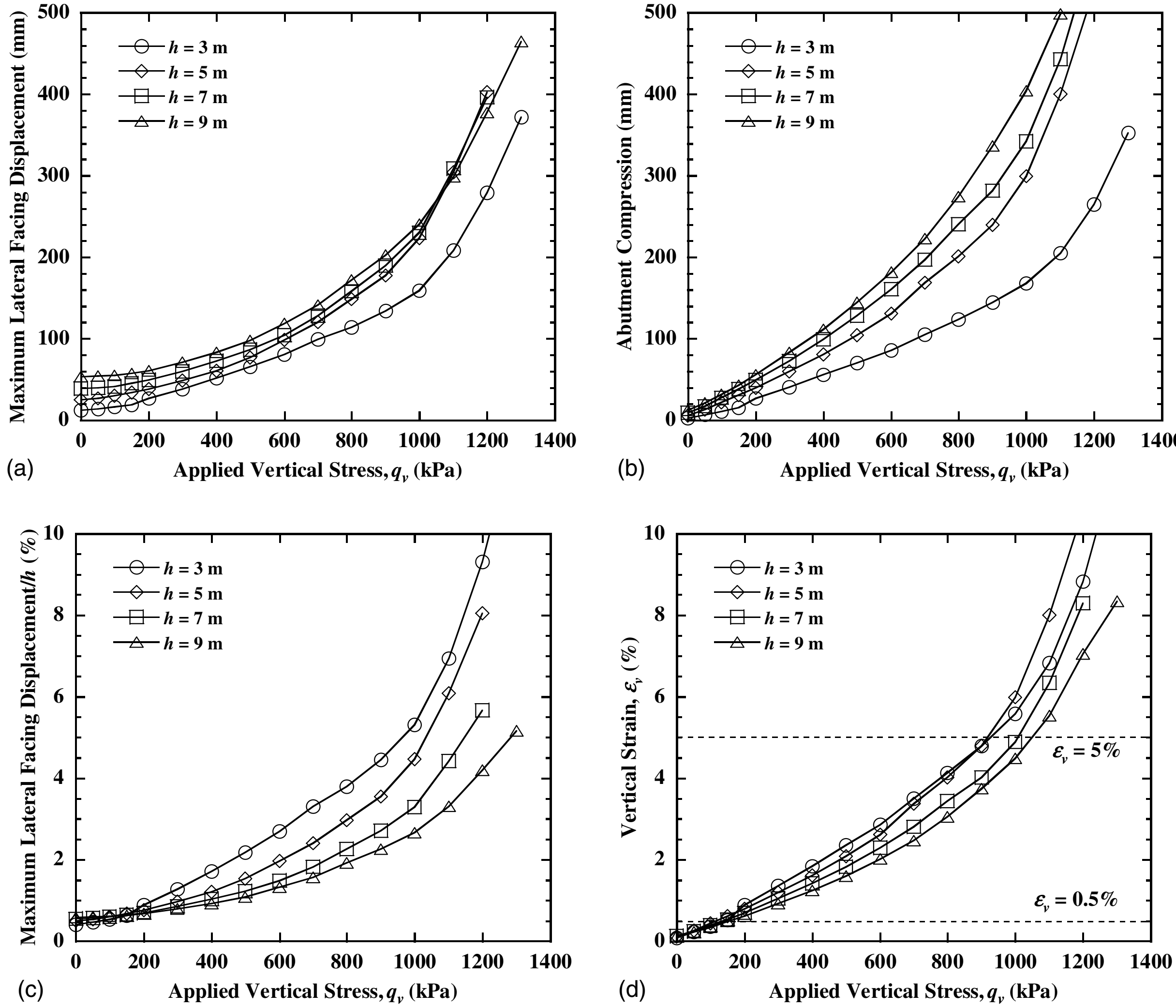

Fig. 16. Effect of lower GRS wall height: (a) maximum lateral facing displacement; (b) abutment compression; (c) normalized maximum lateral facing displacement; and (d) vertical strain.

abutments have a stiffer response. This is attributed to higher average effective stress conditions and associated larger soil stiffness for the taller abutments. The results in Figs. 16(c and d) suggest that, all else being equal, laboratory or field tests conducted on reduced-scale physical models with lower average effective stress conditions may yield conservative (i.e., less stiff) vertical strain relationships for the design of GRS bridge abutments.

Failure Surface

The failure surface for the GRS bridge abutment develops as shear strains increase during the loading stage. Contours of shear strain magnitude for the baseline case at the service limit ($\varepsilon_v = 0.5\%$) and strength limit ($\varepsilon_v = 5\%$) are shown in Fig. 17. At the service limit, shear strains are concentrated at the heel of the bridge seat and suggest a potential failure surface that moves downward from the heel to the toe of the abutment. At the strength limit, the abutment is approaching failure, as manifested by the formation of large shear strain zones. The failure mechanism is a combination of punching shear failure of the bridge seat and internal shear failure of the lower GRS fill. The internal failure surface migrates vertically downward from the heel of the bridge seat to approximately the midheight ($z = h/2$) and then diagonally to the toe of the lower GRS wall. A similar failure surface shape for GRS bridge abutments was identified by Leshchinsky (2014) based on limit analysis.

Following an approach similar to Fig. 17(b), a bilinear failure surface was constructed at the strength limit for each simulation of the parametric study based on contours of shear strain magnitude. These simplified diagrams are presented together for comparison in Fig. 18. In general, the geometry of these surfaces shows close similarity over a wide range of simulated conditions, with some exceptions. The bilinear surface consistently starts at the heel of the bridge seat and migrates downward to the midheight and then diagonally to the toe of the lower GRS wall. Failure surfaces show essentially no effect from changing reinforcement vertical spacing in Fig. 18(a) and similar close agreement for variable geogrid stiffness and geogrid length in Figs. 18(b and c), respectively. The failure surfaces in Fig. 18(d) indicate that the intersection point of the bilinear surface moves downward with an increasing number of secondary reinforcement layers, as might be expected. The failure surfaces in Figs. 18(e–g) indicate that backfill soil cohesion, friction angle, and dilation angle have little effect on failure surface geometry. Conversely, the failure surfaces in Figs. 18(h–j) show that abutment geometry has an important effect. Fig. 18(h)

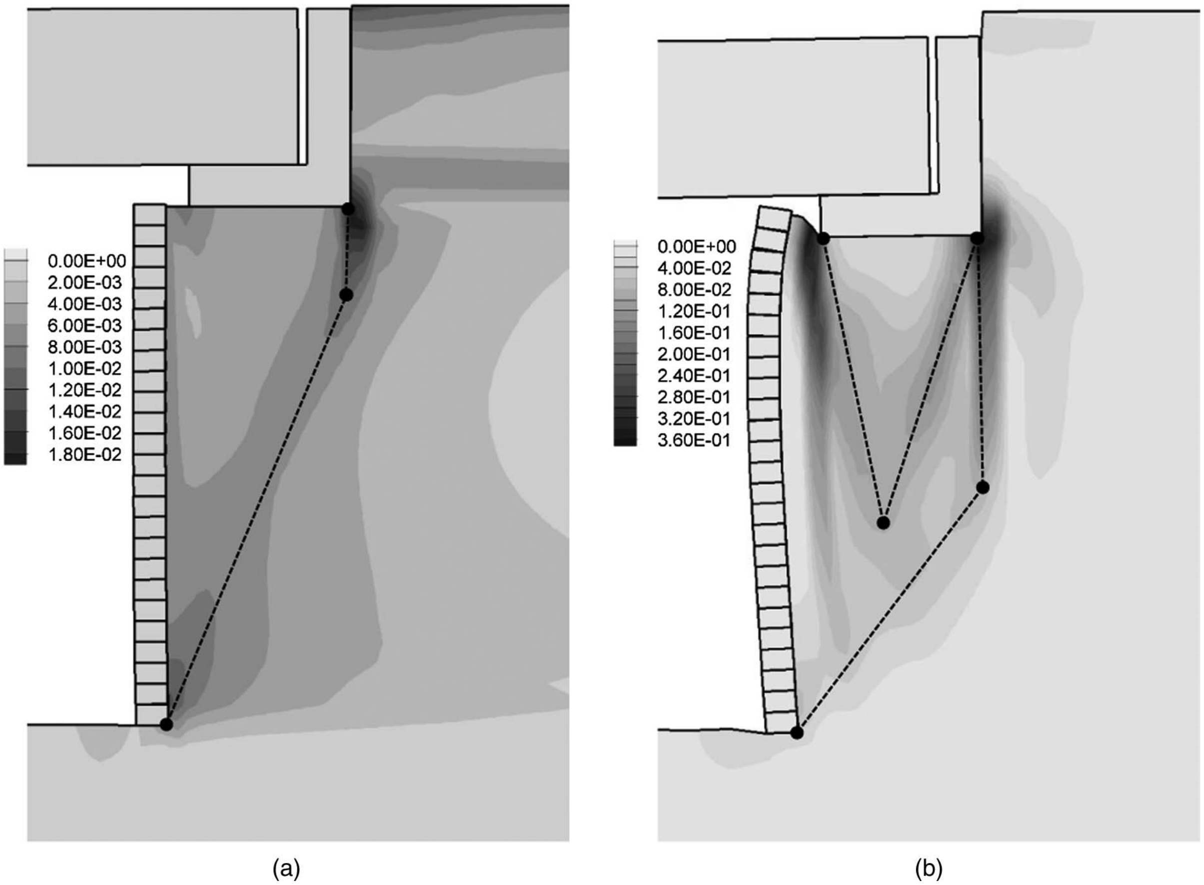

Fig. 17. Contours of shear strain magnitude for baseline case: (a) service limit ($\varepsilon_v = 0.5\%$); and (b) strength limit ($\varepsilon_v = 5\%$).

indicates that increasing the bridge seat setback distance changes the slope of the upper line of the bilinear failure surface but, interestingly, has no effect on the intersection point or lower line for the conditions investigated. Fig. 18(i) indicates that increasing the bridge seat length changes the geometry for both sections of the failure surface, but the vertical elevation of the intersection point remains consistent. Finally, Fig. 18(j) indicates that abutments with lower GRS wall heights of 5, 7, and 9 m have the same relative geometry when plotted as z/h; however, the smaller height of $h =$ 3 m displays a clearly different geometry that is similar in shape to the failure surfaces for abutments with larger a_b and L_s.

Based on the trends in Fig. 18, a general bilinear failure surface is proposed and illustrated in Fig. 19 for GRS bridge abutments with conditions similar to those investigated in the current study. The failure surface starts at the heel of the bridge seat and moves downward to an intersection point at midheight ($z = h/2$) and then diagonally to the toe of the lower GRS wall. The horizontal location of the intersection point is controlled by geometry. For $a_b + L_s \leq h/3$, the upper line is vertical and the intersection point is located at $x = a_b + L_s$. For $a_b + L_s > h/3$, the upper line is not vertical and the intersection point is located at $x = h/3$. The proposed failure surface is predicated on the assumption that secondary reinforcement, if present, is contained within the top half of the lower GRS fill.

Conclusions

A numerical investigation of deformation and failure behavior for GRS bridge abutments was conducted using finite-difference analysis. The backfill soil was characterized using a nonlinear elastoplastic model that incorporates a hyperbolic stress–strain relationship with strain-softening behavior and the Mohr–Coulomb failure criterion. The geogrid reinforcement was characterized using a hyperbolic load–strain–time model. For each numerical simulation, the GRS bridge abutment was constructed in stages, including soil compaction effects, and then monotonically loaded in stages to failure. A parametric study was conducted to investigate the effects of various parameters on abutment deformation and failure behavior. The following conclusions are reached for the conditions investigated in this study:

1. As compared to simulations for elastic–perfectly plastic soil (PPS) and linearly elastic reinforcement (LER), the strain-softening behavior of the backfill soil and nonlinear behavior of the geogrid reinforcement had relatively small effects on abutment deformations at the service limit ($\varepsilon_v = 0.5\%$ or $q_v = 200$ kPa). However, these effects, and especially nonlinear reinforcement, became significant above the service limit leading to the strength limit ($\varepsilon_v = 5\%$). A LER model was able to characterize the deformation behavior of GRS bridge abutments at the service limit, but not for higher applied vertical stress conditions approaching failure. Bearing capacity at the strength limit was slightly overestimated using a PPS model and significantly overestimated using a LER model.
2. Reinforcement vertical spacing, reinforcement stiffness, backfill soil friction angle, and lower GRS wall height had the most significant effects on abutment deformations. The maximum lateral facing displacement and abutment vertical compression decreased significantly with decreasing reinforcement spacing, increasing reinforcement stiffness, and increasing backfill soil

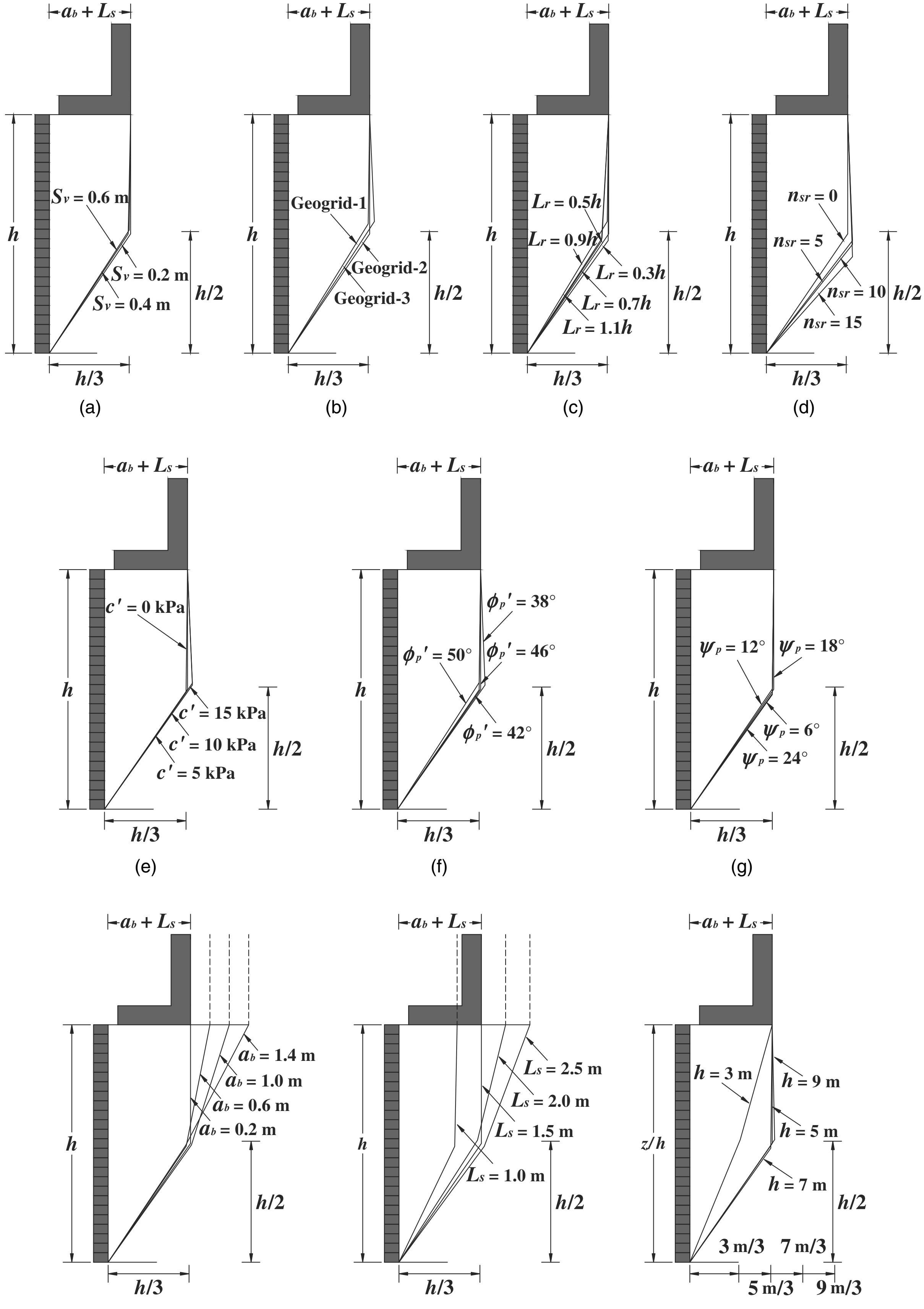

Fig. 18. Bilinear failure surfaces for parametric study: (a) reinforcement vertical spacing; (b) reinforcement stiffness; (c) reinforcement length; (d) secondary reinforcement; (e) backfill soil cohesion; (f) backfill soil friction angle; (g) backfill soil dilation angle; (h) bridge seat setback distance; (i) bridge seat length; and (j) lower GRS wall height.

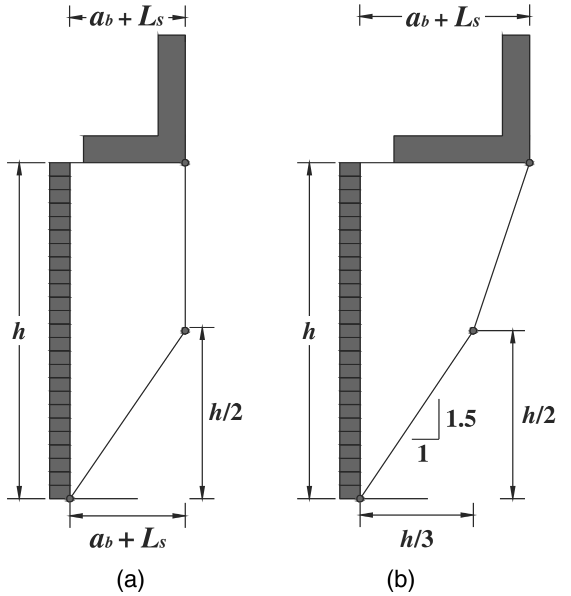

Fig. 19. Proposed general bilinear failure surface for GRS bridge abutments: (a) $a_b + L_s \leq h/3$; and (b) $a_b + L_s > h/3$.

friction angle. As the height of the lower GRS wall increased, the maximum lateral facing displacement and abutment vertical compression increased; however, the normalized maximum lateral facing displacement and vertical strain decreased. Secondary reinforcement had a relatively small effect at the service limit and significantly increased the bearing capacity at the strength limit.

3. Reinforcement and backfill soil properties had little effect on the geometry of the failure surface. Conversely, parameters associated with abutment geometry, such as bridge seat length, bridge seat setback distance, and height of the lower GRS wall, had important effects. The failure surface can be approximated as bilinear, starting at the heel of the bridge seat, moving downward to an intersection point at midheight, and then diagonally to the toe of the lower GRS wall, as illustrated in Fig. 19.

Acknowledgments

Financial support for this investigation was provided by the California Department of Transportation (Caltrans) and is gratefully acknowledged. The authors thank Dr. Charles S. Sikorsky of the Caltrans Office of Earthquake Engineering for his support and assistance with the project and Dr. P. Benson Shing, Professor and Chair of the Department of Structural Engineering at the University of California, San Diego, for several helpful discussions on the design of bridge systems.

Notation

The following symbols are used in this paper:

A_r = reinforcement cross-sectional area;
a_b = bridge seat setback distance;
B = bulk modulus;
c' = soil cohesion;
c_i' = interface adhesion;
D = bridge beam depth;
$d_{\max}$ = soil maximum particle size;
d_e = distance between top facing block and bridge beam;
E = elastic modulus;
E_r = reinforcement elastic modulus;
E_t = soil tangent elastic modulus;
E_{ur} = soil unloading–reloading elastic modulus;
F_v = vertical force per unit width on lower GRS fill;
h = lower GRS wall height;
J_t = reinforcement tangent stiffness;
J_s = reinforcement secant stiffness;
J_0 = reinforcement initial stiffness;
$J_{5\%}$ = reinforcement secant stiffness at 5% strain;
K = elastic modulus number;
K_b = bulk modulus number;
K_p = Rankine passive earth pressure coefficient;
K_{ur} = unloading–reloading modulus number;
k_n = interface normal stiffness;
k_s = interface shear stiffness;
L_b = bridge span;
L_c = contact length between bridge beam and bridge seat;
L_s = bridge seat length;
L_r = reinforcement length;
m = bulk modulus exponent;
n = elastic modulus exponent;
n_{sr} = number of secondary reinforcement layers;
p_a = atmospheric pressure;
q_{ult} = ultimate bearing capacity;
q_v = average applied vertical stress on lower GRS fill;
$q_{0.5\%}$ = average applied vertical stress on lower GRS fill at 0.5% strain;
$q_{5\%}$ = average applied vertical stress on lower GRS fill at 5% strain;
RF = interface shear strength reduction factor;
R_f = failure ratio;
R_{sd} = ratio of bridge beam span to bridge beam depth;
S_v = reinforcement vertical spacing;
T = reinforcement tensile force;
T_{ult} = reinforcement ultimate tensile strength;
$T_{5\%}$ = reinforcement tensile force at 5% strain;
t = time;
t_r = reinforcement thickness;
x = horizontal distance from back side of wall facing;
z = vertical distance above top surface of foundation soil;
γ = soil unit weight;
γ_b = bridge beam unit weight;
$\Delta_{h,200}$ = maximum lateral facing displacement for $q_v = 200$ kPa;
$\Delta_{v,200}$ = average compression of lower GRS fill for $q_v = 200$ kPa;
δ_i' = interface friction angle;
ε = reinforcement tensile strain;
ε_p = soil incremental plastic shear strain;
ε_v = average vertical strain of lower GRS fill;
ν = Poisson's ratio;
ν_t = tangent Poisson's ratio;
σ_c' = effective confining stress;
σ_1' = major principal effective stress;
σ_3' = minor principal effective stress;
ϕ' = soil friction angle;
ϕ_{cv}' = soil constant volume friction angle;

ϕ'_p = soil peak friction angle;
χ = empirical fitting parameter;
ψ = soil dilation angle;
ψ_{cv} = soil constant volume dilation angle; and
ψ_p = soil peak dilation angle.

References

Abu-Hejleh, N., W. Outcalt, T. Wang, and J. G. Zornberg. 2000. *Performance of geosynthetic-reinforced walls supporting the Founders/Meadows Bridge and approaching roadway structures. Report 1: Design, materials, construction, instrumentation and preliminary results*. Rep. No. CDOT-DTD-R-2000-5. Denver: Colorado DOT.

Abu-Hejleh, N., J. G. Zornberg, T. Wang, M. McMullen, and W. Outcalt. 2001. *Performance of geosynthetic-reinforced walls supporting the Founders/Meadows Bridge and approaching roadway structures. Report 2: Assessment of the performance and design of the front GRS walls and recommendations for future GRS bridge abutments*. Rep. No. CDOT-DTD-R-2001-12. Denver: Colorado DOT.

Abu-Hejleh, N., J. G. Zornberg, T. Wang, and J. Watcharamonthein. 2002. "Monitored displacements of unique geosynthetic-reinforced soil bridge abutments." *Geosynth. Int.* 9 (1): 71–95. https://doi.org/10.1680/gein.9.0211.

Adams, M. 1997. "Performance of a prestrained geosynthetic reinforced soil bridge pier." In *Proc., Mechanically stabilized backfill*, 35–53. Rotterdam, Netherlands: Balkema.

Adams, M., J. Nicks, T. Stabile, J. Wu, W. Schlatter, and J. Hartmann. 2011a. *Geosynthetic reinforced soil integrated bridge system interim implementation guide*. FHWA-HRT-11-026. Washington, DC: USDOT.

Adams, M., J. Nicks, T. Stabile, J. Wu, W. Schlatter, and J. Hartmann. 2011b. *Geosynthetic reinforced soil integrated bridge system synthesis report*. FHWA-HRT-11-027. Washington, DC: USDOT.

Adams, M. T., P. S. Ooi, and J. E. Nicks. 2014. "Mini-pier testing to estimate performance of full-scale geosynthetic reinforced soil bridge abutments." *Geotech. Test. J.* 37 (5): 884–894. https://doi.org/10.1520/GTJ20140007.

Allen, T. M., and R. J. Bathurst. 2014a. "Design and performance of 6.3-m-high, block-faced geogrid wall designed using K-stiffness method." *J. Geotech. Geoenviron. Eng.* 142 (2): 04013016. https://doi.org/10.1061/(ASCE)GT.1943-5606.0001013.

Allen, T. M., and R. J. Bathurst. 2014b. "Performance of an 11 m high block-faced geogrid wall designed using the K-stiffness method." *Can. Geotech. J.* 51 (1): 16–29. https://doi.org/10.1139/cgj-2013-0261.

Ambauen, S., B. Leshchinsky, Y. Xie, and D. Rayamajhi. 2015. "Service-state behavior of reinforced soil walls supporting spread seats: A parametric study using finite-element analysis." *Geosynth. Int.* 23 (3): 156–170. https://doi.org/10.1680/jgein.15.00039.

Ardah, A., M. Abu-Farsakh, and G. Voyiadjis. 2017. "Numerical evaluation of the performance of a Geosynthetic Reinforced Soil-Integrated Bridge System (GRS-IBS) under different loading conditions." *Geotext. Geomembr.* 45 (6): 558–569. https://doi.org/10.1016/j.geotexmem.2017.07.005.

Berg, R. R., B. R. Christopher, and N. Samtani. 2009. *Design and construction of mechanically stabilized earth walls and reinforced soil slopes–Volume I*. FHWA-NHI-10-024. Washington, DC: USDOT.

Caltrans. 1994. *Memos to Designers 7-1*. Sacramento, CA: California DOT.

Duncan, J. M., P. Byrne, K. S. Wong, and P. Mabry. 1980. *Strength, stress-strain and bulk modulus parameters for finite element analysis of stresses and movements in soil masses*. Rep. No. UCB/GT/80-01. Berkeley, CA: Univ. of California.

Gotteland, P., J. P. Gourc, and P. Villard. 1997. "Geosynthetic reinforced structures as bridge abutments: Full scale experimentation and comparison with modelisations." In *Proc., Mechanically stabilized backfill*, 25–34. Rotterdam, Netherlands: Balkema.

Guler, E., M. Hamderi, and M. M. Demirkan. 2007. "Numerical analysis of reinforced soil-retaining wall structures with cohesive and granular backfills." *Geosynth. Int.* 14 (6): 330–345. https://doi.org/10.1680/gein.2007.14.6.330.

Hatami, K., and R. J. Bathurst. 2006. "Numerical model for reinforced soil segmental walls under surcharge loading." *J. Geotech. Geoenviron. Eng.* 132 (6): 673–684. https://doi.org/10.1061/(ASCE)1090-0241(2006)132:6(673).

Helwany, S. M. B., J. T. H. Wu, and B. Froessl. 2003. "GRS bridge abutments—An effective means to alleviate bridge approach settlement." *Geotext. Geomembr.* 21 (3): 177–196. https://doi.org/10.1016/S0266-1144(03)00004-9.

Helwany, S. M. B., J. T. H. Wu, and A. Kitsabunnarat. 2007. "Simulating the behavior of GRS bridge abutments." *J. Geotech. Geoenviron. Eng.* 133 (10): 1229–1240. https://doi.org/10.1061/(ASCE)1090-0241(2007)133:10(1229).

Iwamoto, M. K., P. S. Ooi, M. T. Adams, and J. E. Nicks. 2015. "Composite properties from instrumented load tests on mini-piers reinforced with geotextiles." *Geotech. Test. J.* 38 (4): 397–408. https://doi.org/10.1520/GTJ20140181.

Ketchart, K., and J. T. H. Wu. 1997. "Performance of geosynthetic-reinforced soil bridge pier and abutment, Denver, Colorado, USA." In *Proc., Mechanically stabilized backfill*, 101–116. Rotterdam, Netherlands: Balkema.

Lee, K. Z. Z., and J. T. H. Wu. 2004. "A synthesis of case histories on GRS bridge-supporting structures with flexible facing." *Geotext. Geomembr.* 22 (4): 181–204. https://doi.org/10.1016/j.geotexmem.2004.03.002.

Leshchinsky, B. 2014. "Limit analysis optimization of design factors for mechanically stabilized earth wall-supported footing." *Transp. Infrastruct. Geotechnol.* 1 (2): 111–128.

Ling, H. I., S. Yang, D. Leshchinsky, H. Liu, and C. Burke. 2010. "Finite-element simulations of full-scale modular-block reinforced soil retaining walls under earthquake loading." *J. Eng. Mech.* 136 (5): 653–661. https://doi.org/10.1061/(ASCE)EM.1943-7889.0000108.

Liu, H., and H. I. Ling. 2012. "Seismic responses of reinforced soil retaining walls and the strain softening of backfill soils." *Int. J. Geomech.* 12 (4): 351–356. https://doi.org/10.1061/(ASCE)GM.1943-5622.0000051.

Nicks, J. E., M. T. Adams, P. S. K. Ooi, and T. Stabile. 2013. *Geosynthetic reinforced soil performance testing–Axial load deformation relationships*. FHWA-HRT-13-066. Washington, DC: USDOT.

Nicks, J. E., D. Esmaili, and M. T. Adams. 2016. "Deformations of geosynthetic reinforced soil under bridge service loads." *Geotext. Geomembr.* 44 (4): 641–653. https://doi.org/10.1016/j.geotexmem.2016.03.005.

Saghebfar, M., M. Abu-Farsakh, A. Ardah, and Q. Chen. 2017. "Performance monitoring of Geosynthetic Reinforced Soil Integrated Bridge System (GRS-IBS) in Louisiana." *Geotext. Geomembr.* 45 (2): 34–47. https://doi.org/10.1016/j.geotexmem.2016.11.004.

Stein, W. J., and T. R. Neuman. 2007. *Mitigation strategies for design exceptions*. FHWA-SA-07-011. Washington, DC: USDOT.

Vieira, C. S., M. L. Lopes, and L. M. Caldeira. 2013. "Sand-geotextile interface characterisation through monotonic and cyclic direct shear tests." *Geosynth. Int.* 20 (1): 26–38. https://doi.org/10.1680/gein.12.00037.

Walters, D. L., T. M. Allen, and R. J. Bathurst. 2002. "Conversion of geosynthetic strain to load using reinforcement stiffness." *Geosynth. Int.* 9 (5–6): 483–523. https://doi.org/10.1680/gein.9.0226.

Won, G. W., T. Hull, and L. De Ambrosis. 1996. "Performance of a geosynthetic segmental block wall structure to support bridge abutments." In Vol. 1 of *Proc., Earth reinforcement*, 543–548. Rotterdam, Netherlands: Balkema.

Wu, J. T. H., K. Ketchart, and M. Adams. 2001. *GRS bridge piers and abutments*. Rep. No. FHWA-RD-00-038. Washington, DC: USDOT.

Wu, J. T. H., K. Z. Z. Lee, S. B. Helwany, and K. Ketchart. 2006a. *Design and construction guidelines for geosynthetic-reinforced soil bridge abutments with a flexible facing*. NCHRP Rep. 556. Washington, DC: Transportation Research Board.

Wu, J. T. H., K. Z. Z. Lee, and T. Pham. 2006b. "Allowable bearing pressures of bridge sills on GRS bridge abutments with flexible facing."

J. Geotech. Geoenviron. Eng. 132 (7): 830–841. https://doi.org/10.1061/(ASCE)1090-0241(2006)132:7(830).

Wu, J. T. H., and T. Q. Pham. 2013. “Load-carrying capacity and required reinforcement strength of closely spaced soil-geosynthetic composites.” *J. Geotech. Geoenviron. Eng.* 139 (9): 1468–1476. https://doi.org/10.1061/(ASCE)GT.1943-5606.0000885.

Wu, J. T. H., T. Q. Pham, and M. T. Adams. 2013. *Composite behavior of geosynthetic reinforced soil mass*. FHWA-HRT-10-077. Washington, DC: USDOT.

Xie, Y., and B. Leshchinsky. 2015. “MSE walls as bridge abutments: Optimal reinforcement density.” *Geotext. Geomembr.* 43 (2): 128–138. https://doi.org/10.1016/j.geotexmem.2015.01.002.

Yang, K.-H., J. G. Zornberg, C.-N. Liu, and H.-D. Lin. 2012. “Stress distribution and development within geosynthetic-reinforced soil slopes.” *Geosynth. Int.* 19 (1): 62–78. https://doi.org/10.1680/gein.2012.19.1.62.

Yu, Y., R. J. Bathurst, and T. M. Allen. 2016. “Numerical modeling of the SR-18 geogrid reinforced modular block retaining walls.” *J. Geotech. Geoenviron. Eng.* 142 (5): 04016003. https://doi.org/10.1061/(ASCE)GT.1943-5606.0001438.

Zheng, Y., and P. J. Fox. 2016a. “Closure to ‘Numerical investigation of geosynthetic-reinforced soil bridge abutments under static loading.’ By Yewei Zheng and Patrick J. Fox.” *J. Geotech. Geoenviron. Eng.* 143 (4): 07016032. https://doi.org/10.1061/(ASCE)GT.1943-5606.0001623.

Zheng, Y., and P. J. Fox. 2016b. “Numerical investigation of geosynthetic-reinforced soil bridge abutments under static loading.” *J. Geotech. Geoenviron. Eng.* 142 (5): 04016004. https://doi.org/10.1061/(ASCE)GT.1943-5606.0001452.

Zheng, Y., and P. J. Fox. 2017. “Numerical investigation of the geosynthetic reinforced soil-integrated bridge system under static loading.” *J. Geotech. Geoenviron. Eng.* 143 (6): 04017008. https://doi.org/10.1061/(ASCE)GT.1943-5606.0001665.

Zheng, Y., P. J. Fox, and J. S. McCartney. 2017. “Numerical study of compaction effect on the static behavior of geosynthetic reinforced soil-integrated bridge system.” In *Proc., Geotechnical Frontiers 2017*, 33–43. Orlando, FL.

Zheng, Y., P. J. Fox, and P. B. Shing. 2014. “Numerical simulations for response of MSE wall-supported bridge abutment to vertical load.” In *Proc., GeoShanghai 2014, Int. Conf. on Geotechnical Engineering 2014*, 493–502. Reston, VA: ASCE.

Zheng, Y., P. J. Fox, and P. B. Shing. 2015. “Numerical study of deformation behavior for a geosynthetic-reinforced soil bridge abutment under static loading.” In *Proc., IFCEE 2015, Int. Foundations Congress and Equipment Exposition 2015*, 1503–1512. Reston, VA: ASCE.

J. Geotech. Geoenviron. Eng., 2018, 144(7): 04018037